

Role of Ocean Mesoscale Structures in Shaping the Angola-Low Pressure System and the Southern Africa Rainfall

Fabien Desbiolles^{1*, **}, Emma Howard², Ross C. Blamey¹, Rondrotiana Barimalala¹, Neil C.G. Hart², and Chris J.C. Reason¹

¹ *Department of Oceanography, University of Cape Town, South Africa*

² *School of Geography and the Environment, University of Oxford, Oxford, UK*

*Corresponding Author:

fabien.desbiolles@uct.ac.za

**** [Now at Department of Earth and Environmental Sciences, University of Milano - Bicocca](#)**

16 **Abstract**

17 Southern African climate is under the influence of both tropical and subtropical systems
18 which result in a complex region where important interactions co-exist over a large
19 spectrum of spatiotemporal scales. The Angola Low (*AL*), situated on boundary between
20 tropical and subtropical southern Africa, has been diagnosed as a key driver of moisture
21 distribution in the region on daily to seasonal time scales. It has been demonstrated that
22 the *AL* pressure system is sensitive to the dynamics of the neighbouring oceans, but to date
23 no study has considered the model resolution of air-sea interactions required to simulate
24 this sensitivity. Using sensitivity experiments with a regional atmospheric model, which
25 differ only in the mesoscale *SST* forcing characteristics (either the full spectrum of *SST*
26 variability or only its large-scale components are included), we first quantify the importance
27 of *SST* gradients on the Angola Low strength and variability. The results suggest that the
28 mesoscale *SST* variability of the Angola-Benguela Frontal Zone (*ABFZ*) plays a key role in *AL*
29 activity, particularly during the late summer. Synoptic-scale tropical lows, which form the
30 *AL*, are automatically detected, and the results suggest more extreme events occur when
31 the model is forced by mesoscale *SSTs* (everywhere and in the *ABFZ* area only). The rainfall
32 resulting from those events suggests that tropical-low episodes are associated with nearly
33 15% of the total rain in Angola and Namibia. The link between *AL* dynamics and wet spells is
34 also discussed, with the former showing a different spatial pattern as well as frequency
35 when the ocean is fully resolved.

36

37 **Keywords**

38 Mesoscale air-sea interactions, atmospheric dynamics, Angola Low pressure system,
39 southern Africa climate, regional climate simulations.

40 1. Introduction

41 One of the larger challenges facing the climate modeling community in southern
42 Africa is that climate models appear to poorly represent some of the key regional
43 circulation processes and as a result, struggle to produce reasonable simulations of
44 regional rainfall patterns [*Munday and Washington, 2017; Driver et al., 2018*]. The
45 difficulty is partly due to the regional climate of southern Africa being complex and
46 strongly modulated by processes operating on the global scale down to regional and local
47 scales [*Tyson and Preston-Whyte, 2000; Reason et al., 2006*]. Furthermore, due to its
48 geographic position being in the subtropics (south of 10°S), the region straddles the zones
49 dominated by both mid-latitude and tropical weather systems. The narrow, peninsula-like
50 geography of the southern African landmass allows regional ocean phenomena (e.g., the
51 highly variable and dynamic greater Agulhas Current system) to exert a strong influence on
52 rainfall [*Mason, 1995; Reason, 2001*]. These challenges highlight the need for further work
53 on understanding the regional climate dynamics of southern Africa.

54
55 **Figure 1** introduces some of the key features of the atmospheric and oceanic
56 circulation important for southern Africa during the austral summer. Low-level atmospheric
57 synoptic circulation is dominated by semi-permanent subtropical high-pressure cells
58 (orange contours on **Fig. 1**) over both the South Atlantic (Saint Helena High; SAHP) and
59 South Indian Ocean (Mascarene High; *SIOHP*). The latter plays a vital role in regional climate
60 through moisture transport into the continent from the subtropical South Indian Ocean
61 whereas subsidence and alongshore winds associated with the SAHP lead to strong
62 upwelling and cool *SST* along the west coast, keeping western southern Africa dry in
63 summer. However, the ridging of the *SAHP* eastwards along the south coast can lead to
64 significant rainfall over the south and east coastal region of South Africa [*Weldon and*
65 *Reason, 2014; Engelbrecht et al., 2015*].

66
67 Running poleward along eastern South Africa is the warm Agulhas Current (red arrow
68 in **Fig. 1**), which, globally, is one of the most important western boundary currents in terms
69 of its dynamics and variability. Strong air-sea interactions have been identified in the
70 southern Agulhas region, acting on both oceanic and low-level atmospheric dynamics
71 [*Nakamura, 2012; Nonaka et al., 2016; Rouault et al. 2003a; Renault et al., 2017*] and

intensifying storms [Walker and Mey, 1988; Rouault et al., 2002; Singleton and Reason, 2006, 2007]. In Desbiolles et al. [2018], it was shown that the Agulhas eddies and meanders can influence the vertical air column up through the troposphere. These results provide further support for earlier studies that highlight the key role that the Agulhas Current plays in the weather and climate of southern Africa [Jury et al. 1993; Crimp and Mason 1999; Reason and Mulenga, 1999; Reason 2001]. Further north in the western Indian Ocean, there is a strong inflow of moisture towards eastern Africa resulting from the North East Monsoon.

Over the southeastern Atlantic, the resulting alongshore wind associated with the SAHP leads to the divergence of the offshore Ekman current and causes cooling in the upper ocean forming the basis of the well-known Benguela Upwelling System (*BUS*, denoted as “Cool Ocean” in Fig. 1). It has been shown that various spatial scales of the alongshore winds play crucial role in shaping the spatial sea surface temperature (*SST*) pattern along the south-western African coast, from synoptic to small-scale perturbations induced by topography (e.g. Burls and Reason [2008]; Desbiolles et al., [2014; 2016]). The underlying dynamics of the upwelling develops a cold oceanic coastal jet moving northward up to the convergence with the Angola Current. This confluence produces the Angola-Benguela Frontal Zone (hereafter *ABFZ*) where the largest standard deviation in SST in the South Atlantic Ocean is observed (thin black lines in Fig. 1; see also Florenchie et al., 2004). This variability occurs across a range of time scales, at least from decadal (Benguela-Niño, e.g. Shannon et al., 1986, Florenchie et al., [2003]) down to substantial interannual and intraseasonal variability [Hermes and Reason, 2009]. Seasonally, the SST front varies in term of both width and strength. Although the mid-position is relatively stable (around 16.4°S), SST gradients are steepest in austral summer and persist over a wider zonal area [Veitch et al. 2006]. The meridional displacement during the course of the year (about 2° of latitude) is important and can also be highlighted by the standard deviation of the *SST* (Fig. 1). Numerical experiments have shown that the strength and position of the *ABFZ* are sensitive to the SAHP as well as exhibit their own internal variability [Colberg and Reason 2006; 2007].

103 The warm tropical Atlantic basin and its dynamics significantly contribute to regional
104 climate through westerly inflow of moisture into the Angola Low (marked 'L' in **Fig. 1**, and
105 AL hereafter) and help facilitate deep convection in this region [**Mulenga et al, 2003; Cook**
106 **et al., 2004; Reason et al. 2006**]. Shifts in the position or strength of the ABFZ can drive
107 rainfall variability over the adjacent continent [**Reason et al. 2002; Rouault et al. 2003a;**
108 **Hansingo and Reason, 2009**].

109 Rainfall in southern Africa during the summer is produced by a wide array of
110 convective systems, with tropical-extratropical cloud bands typically accounting for the
111 most widespread rainfall across the subcontinent [**Harrison 1984, Hart et al. 2010**]. These
112 cloud bands, locally known as tropical-temperate troughs (**TTT**), often extend diagonally
113 over the subcontinent from southern Angola (near the 'L' region in **Fig. 1**) to the east coast
114 of South Africa and out into the southwest Indian Ocean [**Harrison 1984; Todd and**
115 **Washington 1999; Washington and Todd 1999; Fauchereau et al. 2009; Pohl et al., 2009;**
116 **Hart et al. 2010; Manhique et al. 2011; Hart et al. 2013**]. They have been found to
117 contribute substantially to the seasonal rainfall variability over most countries within
118 southern Africa, including parts of Angola, Botswana, Zambia, Namibia, Zimbabwe,
119 Mozambique and South Africa [**Harrison 1984; Todd and Washington, 1999; Manhique et**
120 **al., 2011, 2015; Crétat et al., 2012; Hart et al., 2013**]. Although the importance of **TTT**s for
121 regional rainfall has been addressed in the literature, there still remains uncertainty
122 regarding the processes that play a role in their formation, frequency and distribution.

123 One key feature of rainfall variability in southern Africa is the presence and strength
124 of the **AL** which appears to play a crucial role in the distribution of moisture across southern
125 Africa, especially into the semi-arid parts. The **AL** is a semi-permanent cyclonic feature
126 occurring during the austral summer, with a peak of activity during the core summer
127 (December-January-February; **DJF** hereafter) and is positioned over the Angola/Namibia
128 border near 17°S [**Mulenga 1998; Mulenga et al., 2003; Howard and Washington 2018;**
129 **Crétat et al., 2018**]. It is still not clear what constrains the **AL** to this particular geographic
130 location during the summer period, but it is possible that topographic features inland of
131 Angola and Namibia (*Serra del Chela* and *Otjihavera* mountain ranges, north and south,
132 respectively; see **Fig.1**), act as a dynamical barrier for the confluence zone of low-level
133 moisture fluxes. The **AL** is characterized here by the minimum of the 850 hPa geopotential
134 height during the austral summer (**Munday and Washington [2017]**, blue dots in **Fig.1**) and

135 is associated with the confluence zone of low-level moisture fluxes originating from tropical
136 and sub-tropical western Indian and tropical Atlantic Oceans (grey arrows in **Fig.1**). Thus,
137 the *AL* dynamics, along with the two high pressure systems located over the adjacent
138 oceans, are viewed as integral in modulating the moisture transport over the southern
139 African region. A stronger (weaker) *AL* has often been linked to an increase (decrease) in
140 rainfall across the region [*e.g. Cook et al. 2004; Reason and Jagadheesha 2005; Reason et*
141 *al. 2006;; Manhique et al. 2015; Munday and Washington 2017*]. Although the large scale
142 drivers have been addressed recently [*e.g., Crétat et al., 2019; Pascale et al., 2019*], the
143 exact mechanisms that influence the strength and location of the *AL* remain poorly
144 understood. In addition, recent studies link the interannual variability of *AL*, in term of
145 strength and position to El-Niño Southern Oscillation (*ENSO*) teleconnections in Southern
146 Africa [*Lyon and Mason 2007*] and provide evidence of links between *AL* variability and
147 subsequent rainfall over southern Africa [*Ratna et al., 2014; Ratnam et al., 2014; Crétat et*
148 *al., 2011; Pohl et al., 2019*]. The phase of the *AL* (i.e. dry heat low versus moist tropical low)
149 may also impact regional rainfall [*Howard and Washington 2018*]. The tropical low phase
150 of the Angola Low is the aggregation of a series of moist-convecting transient cyclonic
151 pressure systems that form in Angola and Zambia and propagate around central and
152 southern Angola. It is therefore paramount to understand and evaluate the mechanisms
153 that influence the formation and evolution of the *AL* and its associated rainfall events.

154 The main processes which affect the strength and position of the *AL* and its moisture
155 supply are still poorly understood and are part of ongoing research. Earlier studies have
156 indicated that the aforementioned *SST* patterns in the neighbouring South Atlantic and
157 Indian Oceans influence southern African climate and rainfall variability [*e.g. Walker, 1990;*
158 *Mason, 1995; Reason, 1998, 1999*]. In particular and closely located to the *AL*, the *ABFZ*,
159 exhibiting strong sub-seasonal variability and important mesoscale *SST* structures, has been
160 identified as a key source region for southern African climate variability. Despite the vast
161 literature on the influence of oceanic large-scale variability on southern African summer
162 rainfall [*e.g., Mason, 1995; Mason and Jury, 1997; Reason and Mulenga, 1999, Behera and*
163 *Yamagata, 2001; Reason, 2001, 2002*], the influences of mesoscale *SST* properties on local
164 weather and climate remain elusive. This paper builds on the contribution of *Desbiolles et*
165 *al. [2018]* by focusing on the specific role that the ocean mesoscale plays in shaping the *AL*
166 system. Through the use of a regional climate model and a suite of sensitivity experiments,

we aim to disentangle the effect of the *ABFZ* variability from the different important mesoscale dynamics of the surrounding oceans.

169
170

171 2. Numerical experiments and Methodology

172

173 The drivers of *AL* dynamics are investigated with the Advanced Research WRF model
174 [Skamarock et al., 2005]. The domain covers the southern African region with an 18km
175 horizontal resolution, extending about from 5°W–70°E and 0°–50°S (see black frame in
176 Fig.1). A total of 51 vertical levels have been used, with half of them sampling the lowest
177 2km to adequately represent Marine Atmospheric Boundary Layer (*MABL*) processes. The
178 initialization is provided by the NCEP Final reanalysis (NCEP-FNL, ~1° spatial resolution) on
179 the 1st August 2008, and the model is first integrated for a month and two days to allow for
180 the spin-up and to define a set of initial conditions (see below) for the subsequent
181 experiments. Following Desbiolles et al. [2018], various experiments are then conducted
182 for the period September 2008 to May 2009, using six-hourly lateral boundary conditions
183 from NCEP-FNL. This study focuses on single austral summer season 2008/2009, which does
184 not corresponding to a year with strong *ENSO* forcing. The reason for this is because strong
185 *ENSO* events have a substantial and nonlinear influence on the weather and climate of
186 southern Africa during the summer months [Lindesay, 1988; Reason et al., 2000] and the
187 paper aims to minimize the potential effects of teleconnections from the tropical Pacific.
188 Nonetheless, the results do suggest the essential role of high resolution *SST* forcing in air–
189 sea interaction processes and hence in regional climate simulations.

190

191 All the experiments described above use the same physical options and
192 parametrization. Namely, the model configuration was set up with the following: the WRF
193 Single-Moment 6-class microphysics scheme [Hong and Lim, 2006]; the Kain-Fritsch cumulus
194 parameterization [Kain and Fritsch, 1990]; the rapid radiative transfer model (RRTM) for
195 long-wave radiation, based on the work by Mlawer et al. [1997]; the Dudhia [1989] scheme
196 for shortwave radiation; the Noah land surface model [Skamarock et al., 2008]. It is widely
197 recognized that the Planetary Boundary Layer (PBL) plays a critical role in mesoscale
198 weather variability. WRF contains several PBL schemes to represent the boundary layer

199 processes and the MYNN2.5 PBL scheme [**Nakanishi and Niino, 2006**] has been chosen for
200 the experiments. These choices correspond to an appropriate combination of
201 parametrizations to take into account air-sea interaction at mesoscales [**Renault et al.,**
202 **2016; Oerder et al., 2016**] even if an underestimation of the coupling coefficient has been
203 reported by **Perlin et al. [2007]**.

204 First, two sets of ensemble-simulation have been carried out, only differing in the
205 prescribed SST forcing (both stem from OSTIA **SS7** observation, **Stark et al., [2007]**). We
206 used the full spectrum of SST variability for the *CTRL* runs and only its large-scale
207 components are included in the *SMTH* simulations. It is worth mentioning here that the
208 daily OSTIA **SS7** product is given on a native grid of 5km of spatial resolution; with a
209 corresponding effective resolution of ~20km [**Desbiolles et al., 2018**]. The SST is then
210 interpolated on the WRF grid (~18km). The *SMTH* boundary conditions have been
211 defined with a low-pass Lanczos filter applied to the *CTRL SS7*, with 2D-half-power filter
212 cut-off wavelengths of 10° (~1000km, in latitude and longitude). The details of the filter
213 used and its consequences are described in **Desbiolles et al. [2018]**. Briefly, the filtered
214 **SS7** fields used to derive the *SMTH* forcing do not include the intermittent features
215 associated with ocean mesoscale eddies and fronts. Mesoscale structures in the
216 following paper correspond then to patterns smaller than ~650km (scale from which **-3**
217 **dB – half power point** – is reached as a result of a transfer function analysis of the filter
218 employed, see **Desbiolles et al., [2018]** for complementary analysis). Some permanent
219 biases persist between the two SST fields, but they have been identified as being
220 equivalent to the ones found in coarser resolution SST datasets usually used to force
221 WRF simulation such as NCEP-FNL. Furthermore, the spatial average of the bias in the
222 two **SS7** forcings (*CTRL* and *SMTH*) is essentially the same (<0.03°C over the summer
223 period). Finally, the *SMTH* forcing field includes a comparable spectral variability to that
224 of commonly used reanalysis products (see **Figs. 2 and 5 of Desbiolles et al. [2018]**).
225 Both sets of experiments correspond to an ensemble of 5 runs integrated with
226 different initial conditions. The latter originate from the 00h00 WRF *CTRL* atmospheric
227 conditions for the 30/08, 31/08, 01/09, 02/09 and 03/09 2008; and are used as initial
228 conditions for *CTRL* and *SMTH* experiments (see **Table I**). It is worth noting that an SST
229 diurnal cycle, estimated from 6-hourly NCEP-FNL, has been added to the daily OSTIA

SST at each model grid point to keep the ocean boundary forcing at the same frequency as its lateral boundaries.

In addition to these two sets of ensemble-simulations, we have combined the two SST forcing fields to isolate the role of the *ABFZ* region from the rest of oceanic domain. First, the *HR-ABFZ* experiment has been forced by the *CTRL SST* in the *ABFZ* Box (defined in **Fig.1**) and the *SMTH* elsewhere. In other words, the *HR-ABFZ* experiment contains the signature of ocean mesoscale eddies and sharp SST gradients in frontal regions and only large-scale SST variability in other oceanic parts of the domain. On the other hand, the *SMTH-ABFZ* experiment is forced by *SST* with ocean mesoscale eddies and sharp gradients; except in the *ABFZ* where the broad *SST* gradient is taken from *SMTH* forcing (see **Fig.2**). Finally, the *SMTH-ABFZ* (which stands for Smoothed-*ABFZ*) experiment will be compared to the *CTRL* run, and conversely the *HR-ABFZ* with the *SMTH* simulations. As for *CTRL* and *SMTH*, a full set of ensembles has been run for both the *HR-ABFZ* and *SMTH-ABFZ* experiments using the initial conditions described above.

Figure 2 and **Table I** summarize the information about the configurations and different runs by showing a snapshot of *SST* for the various experiments and details of the period and forcing of the simulations.

Based on **Howard and Washington [2018]**, we have separated the *AL* into two distinct phases, namely when it has tropical low and when *it has heat low characteristics*. An *AL* event is detected when the cyclonic vorticity reaches a certain threshold (chosen here at $-1.5 \times 10^{-5} \text{ s}^{-1}$) at the 800 hPa pressure level in the region of interest. Due to the noise inherent in the relative vorticity field, a 100km-window low-pass filter has been applied. The latter results in a lobed-shape area of negative vorticity considered to be a substantial convective or *AL* event. This event is then classified as a heat low (tropical low) if its mean low-pass

filtered static stability at 700 hPa is less than (greater than) $2.0 \times 10^{-3} \text{ K/m}$ (see **Howard and Washington [2018]** for more details). Note that the thresholds chosen for the relative vorticity and static stability have been adapted to our simulations. A clear bimodal distribution is obtained in the Probability Density Function (*PDF*) of the static stability at 700 hPa of *AL* events detected of all simulations. The sensitivity of the results to these parameters is discussed in *Section 5*. Consistent with **Howard and Washington [2018]**, the distinction between the two phases of *AL* is more evident in specific humidity values,

confirming that a tropical low (heat low) is characterized by more (less) static stability and wetter (drier) conditions (not shown).

The mean expression of the *AL*, highlighted by the minimum of 850 hPa geopotential height (**Fig.1**), is due to the localized organized convection centers which are mostly active during summer months. To further study the tropical low phase of the *AL*, the TRACK algorithm of **Hodges [1994]** has been applied to the six hourly model output. The methodology of **Howard et al. [2019]** has been followed, which is in turn based on **Hodges et al. [2017]**. To create input data for TRACK, relative vorticity fields at 600, 700 and 800 hPa were smoothed to a resolution of wavelength 210 km, the equivalent of the T63 global grid. As the model output is not global, a discrete cosine transform has been applied, following the methodology of **Woollings et al. [2010]** and **Denis et al. [2002]**. A **Sardeshmukh and Hoskins [1984]** filter was also applied. All cyclonic vorticity maxima with cyclonic relative vorticity exceeding $-5 \times 10^{-6} \text{ s}^{-1}$ were then identified in the vertical average of three pressure levels. The tracks were then generated by first linking these together with a nearest neighbor algorithm, and then, following **Hodges [1999]**, by using an optimization scheme to maximize the track smoothness using adaptive constraints. In order to select continental tropical lows associated with the *AL* from this larger set of cyclones, the following criteria were applied: **(i)** the low must exist over the southern African mainland for all or part of its lifetime, **(ii)** Track longevity must be at least one day; **(iii)** The filtered vertical mean cyclonic relative vorticity must exceed $1.5 \times 10^{-5} \text{ s}^{-1}$ on at least one time-step; **(iv)** There must be coincident cyclonic vorticity in the filtered vorticity at 600, 700 and 800 hPa for 1 time-step; **(v)** The genesis location must not be in the Atlantic, and **(vi)** The genesis location must be north of 25°S . These criteria are consistent with **Howard et al. [2019]** and justified in that paper. In brief, they ensure that the identified tracks are not heat lows, extra-tropical lows, coastally trapped Kelvin waves, or spurious events.

3. The Angola-Low response to Ocean Mesoscale

3.1. The Angola-low system in the *CTRL* run

292 **Figure 3a** shows the *CTRL* ensemble-mean of the 800 hPa geopotential height during
 293 austral summer (*DJF*) in colors and the associated moisture fluxes (arrows). This level is
 294 chosen so as to be just above the interior plateau of southern Africa. The presence of the
 295 *AL* and moisture inflows from the western Indian Ocean and the tropical southeast Atlantic
 296 are apparent. The semi-permanent *AL* cyclonic feature is centered near the Namibia-Angola
 297 border and extends over neighboring Zambia and Botswana in the *CTRL* ensemble-mean
 298 simulations (**Fig.3a**). The summer-mean position and the strength of the *AL* system
 299 depicted here are in agreement with that derived from ERA-Interim reanalyses and CMIP5
 300 models (e.g., *Munday and Washington [2017]; Howard and Washington [2018]*). Moisture
 301 influx from the subtropical South Indian Ocean is facilitated by the *SIOHP* and the
 302 anticyclonic circulation over northern South Africa and southern Mozambique (e.g.,
 303 *Barimalala et al., [2019]*). A weak trough is present in the Mozambique Channel; this
 304 feature is stronger nearer the surface and is sensitive to the height of the topography of
 305 Madagascar [*Barimalala et al., 2018*]).

306 **Figure 3b** summarizes the DJF seasonal features related to *AL* activity in the *CTRL*
 307 simulation. The summer ensemble-mean of the 800hPa geopotential height (i.e. *AL*
 308 location) is plotted as grey contours, the standard deviation of SST forcing field during the
 309 entire simulation is shown in blue contours and the dark blue dots represent the area
 310 where the proxy for deep convection reaches a specific threshold for more than 10% of the
 311 time in the simulation. The deep convection proxy has been defined as an Outgoing
 312 Longwave Radiation (*OLR*) value smaller than 245 W m^{-2} . This magnitude of *OLR* has
 313 previously been used as a proxy for rainfall in the region of interest [e.g., *Fauchereau et al.,*
 314 **2009**]. The NW-SE oriented band extending across southern Africa from the *AL* represents a
 315 typical *TTT* or cloud band axis [*Todd and Washington, 1999; Hart et al., 2010; 2013*].
 316 Furthermore, the three key regions of incoming vertically-integrated moisture flux from the
 317 surface to 800 hPa are depicted in **Fig.3b**.

318 **Figure 4** represents the time evolution of the 30-day window running-mean of the
 319 minimum of the 800 hPa in the *CTRL*, the number of Tropical Low (*TL*) and Heat Low (*HL*)
 320 daily events detected, and the ratio of *TL* events during the period of simulation, in panels
 321 (a), (b) and (c), respectively. The evolution of the *AL*, illustrated in **Figure 4a**, reflects the
 322 seasonality already described with the cyclonic feature more active during the core of
 323 austral summer (*DJF*). The shaded area corresponds to ± 1 standard deviation of the mean

324 *CTRL* ensemble-simulations and will help hereafter to denote a significant difference in the
 325 sensitivity experiments. As mentioned in *Section 2*, we have identified and separated the
 326 two distinct phases of the *AL* and the evolution of dry and wet events are illustrated
 327 together with the ratio of *TL* events compared to the total of *AL* events in **Figures 4b and**
 328 **4c**, respectively. Consistent with **Howard and Washington [2018]**, the formation of a
 329 tropical low is favored during *DJF*, while the transition between dry and moist convective
 330 systems is observed in mid-November. During October and November however, *HL* events
 331 correspond to a strong activity of the *AL* (**Fig. 4**). The *TL* season tends to occur when the
 332 moisture fluxes into the sub-continent from the tropical southeast Atlantic becomes
 333 important. This timing reinforces the view of the *AL* as a part of the confluence zone of
 334 moisture fluxes over tropical southwestern Africa and that this system is the main driver of
 335 rainfall over the sub-continent during the core of austral summer [**Reason et al., 2006**]
 336 (discussed further in *Section 5*). During the austral summer, the low-level atmospheric
 337 circulation favors the inland penetration of moisture from the western Indian and the
 338 tropical southeast Atlantic Oceans (**Fig. 3**). These incoming moisture fluxes are mostly
 339 driven by the large-scale circulation and the presence of the *AL* which lead to low level
 340 convergence of the available moisture there. However, the presence of highlands in Angola
 341 (*Serra de Chela*) and Namibia (*Otjihavera*) can influence the incoming moisture fluxes, and
 342 their convergence as discussed in **Section 5**.

343 Although the objective here is to compare the sensitivity of the different simulations
 344 to the presence or not of mesoscale *SST* variability in the forcing, it should be noted that
 345 the evolution of the main circulation features which drive the southern Africa climate is well
 346 represented by the ensemble *CTRL* simulation (see e.g. the summer mean depicted by ERA-
 347 Interim in **Fig. 1**). Moreover, the rainfall variability and the total precipitation in the *CTRL*
 348 ensemble simulation compare well to TRMM data. The largest bias is seen in the northern
 349 part of the domain (tropical climate) which is not surprising since the model boundary is
 350 close to the Congo basin. However, the model has been configured to reproduce and
 351 simulate the extra-tropical part of Africa. The southern African domain in general shows
 352 relatively small daily rainfall biases between the *CTRL* and TRMM data (less than 1 mm.day⁻¹,
 353 not shown) and the biases between the different sensitivity tests discussed in the following
 354 sections are more important than the biases of *CTRL* with observations. Therefore, we are
 355 confident in using the *CTRL* run as a reference to interpret the sensitivity simulations.

3.2. The Angola-low response to ocean mesoscale eddies and the specific role of the frontal zone.

Figure 5 presents the DJF ensemble-mean 800hPa geopotential height for *CTRL* (a, contour in black), *SMTH* (b, contour in red), *SMTH-ABFZ* (c, contour in blue) and *HR-ABFZ* (d, contour in green). Note that for comparison purpose, contour lines of *CTRL* have been drawn on the panels (b) and (c), and the contour lines of *SMTH* on panel (d). The non-significant statistical difference between the two time series (e.g., the sensitivity experiment with its relative reference) of the geopotential height are denoted in black stippling and result from a student test at the 90% confidence level. The outer 2003m contour height is marked in each panel with the inner contours decreasing at an interval of 1m. **Figure 6** shows the 30-day window running mean (line) and the corresponding standard deviation (shaded) of the minimum of 800hPa geopotential height in the *AL* region of *CTRL* and *SMTH* (a), *CTRL* and *SMTH-ABFZ* (b) and *SMTH* and *HR-ABFZ* (c), respectively.

The *SMTH* simulations, forced by large-scale SST variability only, result in a shift of the *AL* core further to the north (over the eastern part of the Angolan highlands – *Serra de Chela*), which is also weaker compared to the *CTRL* (see **Fig. 5b**). Indeed, 2002 m is the minimum depth of the *AL* in the ensemble-mean *SMTH* while it is 2000 m in *CTRL*. The summer-mean *AL* is then shallower and smaller in areal extent in the *SMTH* compared to *CTRL* ensemble-simulations.

The *CTRL* runs are characterized by a wider spread around the running-mean of the minimum of 800 hPa geopotential height when compared to *SMTH* (shaded areas in **Fig. 6a**). Thus, *SST* forcing which contains mesoscale eddy variability leads to greater intraseasonal fluctuations in the *AL* strength. The mean strength of the *AL* itself is sensitive to ocean mesoscale variability since it is significantly deeper during summer months in the *CTRL* ensemble-simulations. The two curves stray from each other significantly from about December 8th and the 800 hPa geopotential height remains lower in *CTRL* until the end of the simulation (**Fig. 6a**). The largest differences are observed from mid-December to mid-January and in mid-February to mid-March.

The specific role of the *ABFZ* mesoscale variability can be assessed by respectively comparing *CTRL* with *SMTH-ABFZ* and *SMTH* with *HR-ABFZ* (**Figs. 5c, 5d and 6b, 6c**). In the

summer mean, the *AL* is stronger in *CTRL* than in *SMTH-ABFZ* (Figs. 5a, 6b). The minimum value of the 800 hPa geopotential height *DJF* mean is 2000m and 2002m for *CTRL* ensemble-mean and *SMTH-ABFZ*, respectively (Fig. 5c). The core of the cyclonic circulation is slightly farther north in *SMTH-ABFZ* compared to *CTRL*. This result is confirmed by the temporal evolution of the minimum of 800hPa geopotential height and the difference in the strength of the *AL* which is slightly larger from the end of December to the end of January (Fig. 6b). Therefore, removing the mesoscale variability over the *ABFZ* box leads to the *AL* being slightly deeper than *CTRL* during the early summer but shallower or weaker during late December to late January. On the other hand, the addition of mesoscale variability in the *ABFZ* area makes the *AL* season longer, with notably an important difference from mid-February to mid-March (Fig. 6c). The position of the core of the cyclonic circulation is stronger and located farther south in *HR-ABFZ* (Fig. 5d)

Whether or not the *AL* events show heat low or tropical low characteristics does not differ significantly between the various experiments. Even with a stronger *AL* (*CTRL* ensemble-mean, Fig. 6a), the convection leads to *TLs* and *HLs* in the same way. However, a half-month shift in *TL* season seems significant since *TLs* are predominant from mid-November in *CTRL* whereas the corresponding date is early December in *SMTH* (not shown). If all *AL* events produce a relatively similar type of low, the *TLs* admit more extreme values when the *AL* is significantly more important. This result is confirmed by the skewness of the probability distribution function of *TL* events between *CTRL* and *SMTH* (not shown). However, it is not an unexpected result since significant differences between the strengths of the *AL* are found in the core of summer season (Fig. 6a) when *TLs* are favored (Fig. 3c). In other words, a stronger *AL* favors moisture convection and can influence the rainfall distribution and intensity (see Section 4).

412

413 3.3. Possible underlying mechanisms

414

Figure 7a and 7b show a snapshot of the SST gradient corresponding to the *CTRL* and the *SMTH SST* forcing around the *ABFZ* box, respectively. It is worth noting here that the area corresponds approximately to the region where the *SSTs* are combined to create the *SMTH-ABFZ* and the *HR-ABFZ forcing fields*. Figure 7c displays the spatial power spectra of the *CTRL* (black) and *SMTH* (red) *SST* gradients in the *ABFZ* box during the entire simulation.

419

420 The thick lines correspond to an average of each time step spectrum while the thin one
421 corresponds to the fields shown in **Figure 7a** and **7b**.

422 The *SST* gradient plot clearly shows the fine-scale structures present in the *CTRL SST*
423 forcing compared to the *SMTH* one. The presence of ocean mesoscale eddies and fronts
424 leads to a modification of the atmospheric boundary layer through the resulting air-sea
425 temperature differences, air-sea fluxes and thermodynamic adjustment (see e.g. *Desbiolles*
426 *et al. [2018]*). The 2m air temperature gradient is then modified within the same range of
427 scales of the *SSTs* gradients. Here, we observe an important drop off of the *SST* gradient
428 power spectra at about 150km in the *SMTH* forcing compared to *CTRL*, which results in a
429 decrease of energy down to a scale of ~50km (**Figure 7c**). An important drop is also
430 observed in the 2m air temperature horizontal gradient below 200km. However, this scale is
431 typically the range of the atmospheric Rossby radius of deformation [*Orlanski, 1975*] (of
432 order 150 km along the west coast of southern Africa, *Reason and Jury, [1990]*). It has been
433 shown that the variability of air-temperature gradients at these scales plays a crucial role in
434 the near-surface baroclinicity and can then exert significant influence on the large scale
435 circulation [*Nakamura and Yamane, 2010*]. In other words, the spatio-temporal variability
436 of the *ABFZ* influences large scale atmospheric circulation through the near-surface
437 baroclinicity through thermal ocean feedbacks.

438

439

440 4. Tropical low events and associated rainfall variability

441

442 4.1. Tropical Low events, associated circulation and rainfall

443

444 To distinguish the mean expression of the *AL* in high frequency *TL* events, we analyze
445 the events detected by the TRACKS algorithm, which has been specifically adapted for the
446 *AL* system (see **Section 2** and *Howard et al. [2019]* for more details). The algorithm tracks
447 the starting date and the duration of all *TL* events detected in the Angola region for each
448 individual simulation. **Figure 8** compiles statistics of the maximum of the filtered cyclonic
449 vorticity during each event (grouped here for each ensemble member). It is worth noting
450 that the filtered vorticity represents a proxy of the intensity of a cyclonic event; the larger
451 the vorticity (negative because it is a cyclonic event), the more intense the event.

As already seen in *Section 3.2*, all ensemble-simulations produce an equivalent number of *TL* events (not shown) and these events are mainly detected all through the summer season (from November to April). The boxplots of the intensity of the events (**Fig. 8**) show that the mesoscale variability of the ocean (i.e., eddies and fronts) tends to increase the extreme values of the vorticity and thus the intensity of *TL* events. This is particularly seen when comparing *CTRL* and *SMTH* (in which the ocean mesoscale features have been removed over the entire domain). More interestingly, *TL* events depict more extreme values in *HR-ABFZ* and *CTRL* than in *SMTH* and *SMTH-ABFZ* respectively. In other words, the mesoscale features of the ABFZ tend to increase the intensity of cyclonic events of the *AL*. Indeed, more extreme vorticity values are recorded in the *CTRL* than in *SMTH-ABFZ*, and in *HR-ABFZ* than in *SMTH*, respectively (**Fig. 8**). These results are also supported by the second quantiles of the intensity of the events.

Figure 9 shows the composite of the moisture flux (arrows) and daily rainfall during the time step following each *TL* genesis for *CTRL*. The mean *OLR* values lower than the threshold of 250 W/m² are represented by black dots. **Figure 10** shows the anomalies of the composite of daily rainfall associated with *TL* events between *CTRL* and *SMTH* (a), *CTRL* and *SMTH-ABFZ* (b) and *SMTH* and *HR-ABFZ* (c), respectively. Only anomalies for which the Wilcoxon signed rank test p-value [*Wilcoxon*, 1945] are larger than 0.05 are displayed, the remaining areas are shown as hatching.

The composite field of the *CTRL* ensemble-simulation has been constructed by using the time step after the genesis of each *TL* events of all ensemble members. The regional circulation corresponding to a typical *TL* event is characterized by a strong *AL* system with strong incoming moisture flux from the Mozambique Channel and to a lesser extent from the tropical South East Atlantic and tropical western Indian Oceans (**Fig. 9**). Also, there is a substantial anticyclonic moisture transport over central southern Africa into South Africa, producing favorable rainfall conditions over eastern South Africa. These results are robust since all composites display these same common features (*not shown*). Moreover, *TL* events are associated with considerable rainfall over western Angola (**Fig. 9**). However, differences between composite rainfall patterns exist between the individual ensembles. The *CTRL* simulation exhibits high total rainfall over most of Angola, extending to the border of Namibia and Zambia, to the south and east, respectively, whereas in *SMTH* the rainfall

associated with *TL* events is confined to western Angola (*not shown*). The *CTRL* simulation is then wetter near the border of the three neighbouring countries and over the location of the core of the *AL* compared to *SMTH* (**Fig. 10a**). This result is likely related to the location of the genesis of the *TL* events, which is, on average, further west and north in *SMTH* (*not shown*). The latter result is not surprising since it follows the average manifestation of the *AL* system during summer months (**Fig. 5**). The withdrawal of the mesoscale eddies and sharp fronts in the *ABFZ* box leads to reduced rainfall over the coastal part of Angola and near the boundary between southeastern Angola, Namibia and northwestern Botswana (**Fig. 10b**). These areas correspond to the main differences observed in the average expression of the *AL* (**Fig. 5c**). It is important to also note a reduction in the rainfall in *SMTH-ABFZ* compared to *CTRL* (**Fig. 10b**). The latter can be attributed to a substantial increase of *OLR* values (*not shown*) associated with *TTTs*. The addition of ocean mesoscale eddies in the *SST* forcing of the *ABFZ* leads to a North/South shift of the rainfall. This dipole pattern is linked to the location of the *AL* in the *HR-ABFZ* ensemble simulation, where the system is located more southeastward compared to *SMTH* (see **Fig. 5d**). The *HR-ABFZ* is also wetter in Botswana, Zimbabwe and Mozambique during associated *TL* events compared to *SMTH* (**Fig. 10c**).

The rainfall associated with *TL* events represents more than 15% of the total summer rainfall but occurs less than 3% of the time over Angola (*not shown*). This result is consistent for all ensemble simulations. The high-frequency *TL* events thus strongly contribute to the rainfall variability in Angola, both inland and also in the coastal area. This contribution is also true for inland Namibia and Botswana, where the rainfall associated with *TL* represents between 5 - 10% of the total summer rainfall of the entire period.

507

508

4.2. Link to wet and dry spells over southern Africa

510

Given its significance for agriculture and water resource management, it is also of interest to analyse the rainfall variability in terms of changes in wet/dry spells. The wet spell events over southern Africa mostly result from rainfall associated with *TTTs* that emerge within *TL* episodes of the *AL*. In this paper, a wet (dry) spell is defined as a 5 consecutive day period during which the rainfall is more (less) than 1 mm per day. This

definition has been used in previous studies of intraseasonal variability in observed rainfall over various regions of southern Africa (see e.g., *Usman and Reason [2004]; Reason et al., [2005]; Hachigonta and Reason, [2006]*)

Figure 11 shows the *CTRL* ensemble-mean of the total number of wet spell events and **Figure 12** displays the anomalies of the numbers of wet spells found in all the sensitivity experiments compared to *CTRL* and *SMTH* for *SMTH-ABFZ* and *HR-ABFZ*, respectively. Only the significant anomalies are displayed which are defined as an anomaly greater or lower than the standard deviation of the number of events found in the ensemble *CTRL* and/or *SMTH*.

Over the continental area, persistent wet spells (i.e., more than 5 days in a row) are mainly localized over the *AL* and eastern South Africa / Lesotho (near the Drakensberg and Maluti mountains) in all simulations. This pattern is also displayed in the *CTRL* ensemble-simulation in **Figure 11**. Another area of high wet spell frequency occurs over the east coast and northwestern regions of Madagascar. It is likely related to the easterly trade wind and northwest monsoonal flow over the island. Elsewhere, greater wet spell frequency seems mainly related to the *AL* and the development of cloud bands since there is a NW-SE oriented pattern of relatively high frequency extending from western Angola towards the coast of southeastern South Africa. This pattern follows the general description of *TTT* events [*Hart et al., 2012*].

When the ocean simulations do not contain mesoscale *SST* variability, the number of wet spells are significantly reduced within Zimbabwe and southern Mozambique (**Fig. 12a**). Moreover, this result is enhanced and more pronounced when the ocean variability is only removed over the *ABFZ* region (**Fig. 12b**). We also found significantly less wet spells over much of Angola, Namibia as well as parts of the Congo when the ocean variability is removed over the *ABFZ* region. This result can be related to the stronger *AL* found in *CTRL* compared to *SMTH-ABFZ*. The addition of ocean mesoscale variability in the *ABFZ* region (*SMTH* vs. *HR-ABFZ*) leads to large scale amplified rainfall response over the sub-continent except in the coastal Namibia and western South Africa, both of which receive much less rain in summer on average than the rest of the region.

The same analysis can be done for the dry spells which correspond to a persistent (more than 5 days) period of no precipitation. These spells mainly occur over southwestern

547 South Africa, an austral winter rainfall region as well as over southern Mozambique and, not
548 surprisingly, near subtropical high pressure systems over oceans (not shown). The same
549 methodology has been applied to extreme rainfall events and the spatial patterns of
550 anomalies are quite similar to the ones interpreted for the wet spell differences.

551

552

553 **5. Discussion and concluding remarks**

554

555 In this paper, we have highlighted the role of the ocean mesoscale *SST* forcing on the
556 Angola-Low pressure system. The latter contributes strongly to the seasonal variability of
557 austral summer rainfall over the southern Africa continent and is the source region for the
558 major synoptic summer rainfall producing system, the tropical temperate trough or tropical
559 extratropical cloud band. It is therefore important to study the underlying mechanisms of
560 the development and the activity of the *AL*, particularly as its representation in global
561 climate models is important for the rainfall biases exhibited by these models and for future
562 climate projections [Munday and Washington 2017].

563 The results presented here imply that the *AL* appears to be sensitive to whether or
564 not the *SST* imposed at the ocean boundary of the model contains mesoscale variability.
565 Indeed, the *AL* is stronger and deeper in the *CTRL* simulations compared to the *SMTH* one.
566 This difference is especially true in the core of the austral summer (in January, see **Fig. 3**).
567 The core of the *AL* is located farther north in the *SMTH* simulation. The mesoscale *SST*
568 variability of the *ABFZ*, which has been isolated by the *SMTH-ABFZ* and *HR-ABFZ*
569 simulations, acts as well on the location and the intensity of the *AL*. We show that,
570 removing the mesoscale *SST* variability of the oceanic fronts and associated eddies in the
571 *ABFZ* region tends to weaken the strength of the *AL*. By comparing the *SMTH* and *HR-ABFZ*
572 experiments, we have also shown that adding the mesoscale *SST* variability in the *ABFZ*
573 makes the *AL* season longer since it now is evident in strength well into late summer.
574 However, whether or not the *AL* assumes heat low or tropical low characteristics, does not
575 seem sensitive to the spectral content of the *SST* forcing. It is seen that the tropical low
576 season tends to start later (earlier) when the model is forced by mesoscale (large-scale
577 only) *SST* patterns. The latter differences are small and are not significant. However, the
578 *CTRL* ensemble simulations show more intense tropical low events or episodes and the

579 associated rainfall variability response is important since the number of wet spells are
580 enhanced in the region most likely influenced by *TTTs*, the major summer rainfall systems in
581 southern Africa.

582 The mesoscale variability of oceans acts on the marine planetary boundary layer
583 dynamics through thermodynamic processes. The upscaling effect of the local equilibrium
584 between the two fluids at their interface is important in regional atmospheric model
585 simulations in term of seasonal circulation [*Desbiolles et al., 2018*]. However, the full
586 feedback loop is still not resolved in this study since the real world ocean currents can act
587 strongly on *SST* patterns and then on surface and upper-surface winds [*Renault et al.,*
588 **2017**]. The specific role of the *ABFZ*, partly discussed in this paper, and the air-sea
589 interactions over the front are still poorly understood and highlight the need for further
590 investigation. The statistical responses of the surface wind to *SST* changes, analyzed by
591 computing the wind speed perturbation over *SST* perturbations, show a significant linear
592 relationship (*not shown*) but with one order of magnitude lower than the one found in the
593 Agulhas region using observations (e.g., *O'Neill et al., [2005]; Desbiolles et al., [2017]*) or
594 WRF model simulations (*Desbiolles et al. [2018]*).

595 As shown in *Desbiolles et al., [2018]*, the moisture fluxes entering southern Africa
596 from the tropical southeast Atlantic and from the Indian Ocean are sensitive to whether or
597 not there is mesoscale variability present in the *SST* forcing. The incoming fluxes from the
598 tropical Atlantic are reduced by about 10% in the *CTRL* compared to *SMTH* experiments.
599 This reduction is partially due to the *ABFZ* because it is also seen in the differences between
600 the *SMTH* and the *HR-ABFZ* simulations (*not shown*). The presence of sharp *SST* gradients
601 tends to modify the air column enough to remotely reduce the incoming moisture fluxes
602 inland and farther north. As already commented in *Desbiolles et al. [2018]*, the incoming
603 moisture fluxes are also modified in the tropical Indian Ocean (decrease of ~20% in *CTRL*)
604 and through the Mozambique Channel (increase of ~10% in *CTRL*). Not surprisingly, non-
605 significant differences are noticed in the Indian Ocean between *CTRL* and *SMTH-ABFZ* on
606 one hand and between *SMTH* and *HR-ABFZ* on the other hand (*not shown*). With the
607 presence of mesoscale *SSTs*, the *AL* is significantly stronger (**Fig. 5a**) but the incoming
608 moisture flux is weaker through the tropical South East Atlantic. It is worth noting that the
609 800hPa geopotential height is significantly more correlated to the incoming moisture fluxes
610 from the Mozambique Channel (~0.6) than it is to the fluxes originating from elsewhere

611 (~0.2 and ~0.3 for the tropical western Indian and tropical South East Atlantic, respectively,
612 *not shown*). The difference in incoming moisture flux from the tropical South East Atlantic
613 can be explained by the latent heat flux anomalies in the *ABFZ* region and farther north in
614 the tropical Atlantic (*not shown*). Indeed, these anomalies indicated an enhancement of
615 evaporation when the ocean does not contain mesoscale variability. Not surprisingly, the
616 latent heat flux anomalies globally correspond to the anomalies of *SST*, with a large positive
617 anomaly in the *ABFZ* region. More interestingly, the latent heat flux anomalies are
618 important in the *ABFZ* area as well as to its north. This result indicates that the southward
619 low-level atmospheric flow is strongly affected by the presence of sharp *SST* fronts and it is
620 modified beyond the region where the SST forcing has been changed. The effect of ocean
621 mesoscale eddies and frontal activity on the large-scale atmospheric circulation is partially
622 explained by the near-surface baroclinicity enhanced in the mesoscale SST forcing
623 simulations. Indeed, the oceanic thermal feedback in the presence of mesoscale eddies
624 favors horizontal air-temperature gradient at the scale corresponding to the atmospheric
625 Rossby radius of deformation. The structures which have spatial scales similar to the
626 deformation radius can exert a significant influence on the large-scale atmospheric flow
627 [*Nakamura and Yamane, 2010*].

628 An important next step would be to further investigate the moisture sources of the
629 *AL*. Indeed, if the incoming flux is greater in *SMTH* than in *CTRL*, the South Atlantic source of
630 moisture of the *AL* still has to be quantified properly. The source and the retention of
631 moisture in the *AL* system can be studied with Lagrangian experiments to quantify the
632 relative importance of the three moisture flux paths into southern Africa and is part of
633 ongoing work.

634

635 **Acknowledgment**

637 We thank two anonymous reviewers for their valuable contributions that allowed us to
638 improve the manuscript substantially. This research is supported by the Future Climate for
639 Africa UMFULA project, with financial support from the U.K. Natural Environment Research
640 Council (NERC), NE/M020207/1, and the U.K. Government's Department for International
641 Development (DfID). FD, NH, Rbl., Rba., EH and CJCR are directly linked to the project.
642 Support for this study has also been provided by NRF for FD, RBL., RBa., and CJCR, Oxford
643 University for NH. EH is supported by the Origin Foundation John Monash Scholarship. All
644 data used in this study are freely available by the following ftp or url, namely, OSTIA SST
645 ([ftp://podaac-ftp.jpl.nasa.gov/allData/ghrsst/data/L4/GLOB/UKMO/OSTIA/GLOB/UKMO/](ftp://podaac-ftp.jpl.nasa.gov/allData/ghrsst/data/L4/GLOB/UKMO/OSTIA/GLOB/UKMO/OSTIA/)
646 [OSTIA/](ftp://podaac-ftp.jpl.nasa.gov/allData/ghrsst/data/L4/GLOB/UKMO/OSTIA/GLOB/UKMO/OSTIA/)), All simulations have been run on the national UK Cluster ARCHER.

647 **References**

- 648
- 649 Barimalala, R, Desbiolles F., Blamey R., and Reasons C.J.C (2018). The South Indian Ocean
650 Convergence Zone: role of the topography of Madagascar. *Geophysical Research Letters*,
651 45, 11380-11389
- 652
- 653 Barimalala, R., Blamey, R. C., Desbiolles, F., & Reason, C. J. (2019). Variability in the
654 Mozambique Channel Trough and impacts on southeast African rainfall. *Journal of*
655 *Climate*, 33, 749-765, (2019).
- 656
- 657 Behera, S. K., & Yamagata, T. (2001). Subtropical SST dipole events in the southern Indian
658 Ocean. *Geophysical Research Letters*, 28(2), 327-330.
- 659
- 660 Burls, N., & Reason, C. J. C. (2008). Modelling the sensitivity of coastal winds over the
661 Southern Benguela upwelling system to different SST forcing. *Journal of Marine*
662 *Systems*, 74(1-2), 561-584.
- 663
- 664 Colberg, F., & Reason, C. J. C. (2006). A model study of the Angola Benguela Frontal Zone:
665 Sensitivity to atmospheric forcing. *Geophysical research letters*, 33(19).
- 666
- 667 Colberg, F., & Reason, C. J. C. (2007). Ocean model diagnosis of low-frequency climate
668 variability in the South Atlantic region. *Journal of Climate*, 20(6), 1016-1034.
- 669
- 670 Crétat, J., C. Macron, B. Pohl, and Y. Richard (2011), Quantifying internal variability in a
671 regional climate model: A case study for Southern Africa, *Clim. Dyn.*, 37, 1335– 1356
- 672
- 673 Crétat, J., Richard, Y., Pohl, B., Rouault, M., Reason, C., & Fauchereau, N. (2012). Recurrent
674 daily rainfall patterns over South Africa and associated dynamics during the core of the
675 austral summer. *International Journal of Climatology*, 32(2), 261-273.
- 676
- 677 Crétat, J., Pohl, B., Dieppois, B., Berthou, S., & Pergaud, J. (2019). The Angola Low:
678 relationship with southern African rainfall and ENSO. *Climate Dynamics*, 52(3-4), 1783-
679 1803.
- 680
- 681 Dee, D. P., Uppala, S. M., Simmons, A. J., Berrisford, P., Poli, P., Kobayashi, S., Andrae, U.,
682 Balmaseda, M. A., Balsamo, G., Bauer, P., Bechtold, P., Beljaars, A. C. M., van de Berg, L.,
683 Bidlot, J., Bormann, N., Delsol, C., Dragani, R., Fuentes, M., Geer, A. J., Haimberger, L.,
684 Healy, S. B., Hersbach, H., Hólm, E. V., Isaksen, L., Kållberg, P., Köhler, M., Matricardi, M.,
685 McNally, A. P., Monge-Sanz, B. M., Morcrette, J.-J., Park, B.-K., Peubey, C., de Rosnay, P.,
686 Tavolato, C., Thépaut, J.-N. and Vitart, F. (2011), The ERA-Interim reanalysis:
687 configuration and performance of the data assimilation system. *Q.J.R. Meteorol. Soc.*,
688 137: 553–597. doi: HYPERLINK "<http://doi.org/10.1002/qj.828>"10.1002/qj.828
- 689
- 690 Denis, B., Côté, J., & Laprise, R. (2002). Spectral decomposition of two-dimensional
691 atmospheric fields on limited-area domains using the discrete cosine transform (DCT).
692 *Monthly Weather Review*, 130(7), 1812-1829.
- 693

Desbiolles, F., Blanke, B., Bentamy, A., & Grima, N. (2014). Origin of fine-scale wind stress curl structures in the Benguela and Canary upwelling systems. *J. Geophys. Res.: Oceans*, 119(11), 7931-7948.

Desbiolles, F., Blanke, B., Bentamy, A., Roy, C. (2016). Response of the Southern Benguela upwelling system to fine-scale modifications of the coastal wind. *J. Mar. Syst.* **156**, 46–55.

Desbiolles, F., Blamey, R.C., Illig, S., James, R., Barimalala, R., Renault, L., and Reason, C.J.C. [2018], Upscaling impact of Wind/SST mesoscale interactions on southern Africa Summer Climate. *Int. J. of Climatology*

Driver, P., Abiodun, B., & Reason, C. J. C. (2018). Modelling the precipitation response over southern Africa to the 2009–2010 El Niño using a stretched grid global atmospheric model. *Climate Dynamics*, 1-21.

Dudhia, J. (1989). Numerical study of convection observed during the winter monsoon experiment using a mesoscale two-dimensional model. *Journal of the atmospheric sciences*, 46(20), 3077-3107.

Engelbrecht, F., Adegoke, J., Bopape, M. J., Naidoo, M., Garland, R., Thatcher, M., ... & Gatebe, C. (2015). Projections of rapidly rising surface temperatures over Africa under low mitigation. *Environmental Research Letters*, 10(8), 085004.

Fauchereau, N., Pohl, B., Reason, C. J. C., Rouault, M., & Richard, Y. (2009). Recurrent daily OLR patterns in the Southern Africa/Southwest Indian Ocean region, implications for South African rainfall and teleconnections. *Climate Dynamics*, 32(4), 575-591.

Florenchie, P., Lutjeharms, J. R., Reason, C. J. C., Masson, S., & Rouault, M. (2003). The source of Benguela Niños in the south Atlantic Ocean. *Geophysical Research Letters*, 30(10).

Florenchie, P., Reason, C. J. C., Lutjeharms, J. R. E., Rouault, M., Roy, C., & Masson, S. (2004). Evolution of interannual warm and cold events in the southeast Atlantic Ocean. *Journal of Climate*, 17(12), 2318-2334.

Hachigonta, S., & Reason, C. J. C. (2006). Interannual variability in dry and wet spell characteristics over Zambia. *Climate Research*, 32(1), 49-62.

Hart, N. C. G., Reason, C. J. C., & Fauchereau, N. (2010). Tropical–extratropical interactions over southern Africa: Three cases of heavy summer season rainfall. *Monthly weather review*, 138(7), 2608-2623.

Hart, N. C., Reason, C. J., & Fauchereau, N. (2013). Cloud bands over southern Africa: seasonality, contribution to rainfall variability and modulation by the MJO. *Clim. Dyn.*, 41(5-6), 1199-1212.

Hansingo, K., & Reason, C. J. C. (2009). Modelling the atmospheric response over southern Africa to SST forcing in the southeast tropical Atlantic and southwest subtropical Indian

Oceans. *International Journal of Climatology: A Journal of the Royal Meteorological Society*, 29(7), 1001-1012.

Hermes, J. C., & Reason, C. J. C. (2009). Variability in sea-surface temperature and winds in the tropical south-east Atlantic Ocean and regional rainfall relationships. *International Journal of Climatology*, 29(1), 11-21.

Hong, S.-Y., and J.-O. J. Lim, 2006: The WRF Single-Moment 6-class Microphysics scheme (WSM6). *J. Korean Meteor. Soc.*, 42, 129–151.

Hodges, K. I. (1994). A general method for tracking analysis and its application to meteorological data. *Monthly Weather Review*, 122(11), 2573-2586.

Howard, E., & Washington, R. (2018). Characterising the Synoptic Expression of the Angola Low. *Journal of Climate*.

Howard, E. R., Washington, R., & Hodges, K. (2019). Tropical lows in southern Africa: tracks, rainfall contributions and the role of ENSO. *Journal of Geophysical Research: Atmospheres*.

Kain, J. S., & Fritsch, J. M. (1990). A one-dimensional entraining/detraining plume model and its application in convective parameterization. *Journal of the Atmospheric Sciences*, 47(23), 2784-2802.

Lindesay, J. A. (1988). South African rainfall, the Southern Oscillation and a Southern Hemisphere semi-annual cycle. *Journal of Climatology*, 8(1), 17-30.

Lyon, B., & Mason, S. J. (2007). The 1997–98 summer rainfall season in southern Africa. Part I: Observations. *Journal of Climate*, 20(20), 5134-5148.

Mason S. 1995. Sea-surface temperature-South African rainfall associations, 1910-1989. *Int. J. Climatol.* **15**: 119-135.

Mason, S. J., & Jury, M. R. (1997). Climatic variability and change over southern Africa: a reflection on underlying processes. *Progress in Physical Geography*, 21(1), 23-50.

Mlawer, E. J., Taubman, S. J., Brown, P. D., Iacono, M. J., & Clough, S. A. (1997). Radiative transfer for inhomogeneous atmospheres: RRTM, a validated correlated-k model for the longwave. *Journal of Geophysical Research: Atmospheres*, 102(D14), 16663-16682.

Munday, C., & Washington, R. (2017). Circulation controls on southern African precipitation in coupled models: the role of the Angola Low. *Journal of Geophysical Research: Atmospheres*, 122(2), 861-877.

Manhique, A. J., Reason, C. J. C., Rydberg, L., & Fauchereau, N. (2011). ENSO and Indian Ocean sea surface temperatures and their relationships with tropical temperate troughs over Mozambique and the Southwest Indian Ocean. *International Journal of Climatology*, 31(1), 1-13.

- Manhique, A. J., Reason, C. J. C., Silinto, B., Zucula, J., Raiva, I., Congolo F., & Mavume A.F., (2015). Extreme rainfall and floods in southern Mozambique in January 2013, and associated circulation patterns. *Natural Hazards*, 77, 679-691.
- Mason, S. J. (1995). Sea-surface temperature—South African rainfall associations, 1910–1989. *International Journal of Climatology*, 15(2), 119-135.
- Mulenga, H.M., M. Rouault and C.J.C. Reason, 2003: Dry summers over NE South Africa and associated circulation anomalies, *Climate Research*, 25, 29-41.
- Nakamura, M. (2012). Impacts of SST anomalies in the Agulhas Current system on the regional climate variability. *Journal of Climate*, 25(4), 1213-1229.
- Nakamura, M., & Yamane, S. (2010). Dominant anomaly patterns in the near-surface baroclinicity and accompanying anomalies in the atmosphere and oceans. Part II: North Pacific basin. *Journal of Climate*, 23(24), 6445-6467.
- Nakanishi, M., and H. Niino, 2006: An improved Mellor–Yamada Level-3 model: Its numerical stability and application to a regional prediction of advection fog. *Bound.-Layer Meteor.*, 119, 397–407, doi:10.1007/s10546-005-9030-8.
- Nonaka, M., Sasai, Y., Sasaki, H., Taguchi, B., & Nakamura, H. (2016). How potentially predictable are midlatitude ocean currents?. *Scientific reports*, 6, 20153.
- Oerder, V., Colas, F., Echevin, V., Codron, F., Tam, J., & Belmadani, A. (2015). Peru-Chile upwelling dynamics under climate change. *J. Geophys. Res: Oceans*, 120(2), 1152-1172.
- Orlanski, I. (1975). A rational subdivision of scales for atmospheric processes. *Bulletin of the American Meteorological Society*, 527-530.
- Pascale, S., Pohl, B., Kapnick, S. B., & Zhang, H. (2019). On the Angola Low Interannual Variability and Its Role in Modulating ENSO Effects in Southern Africa. *Journal of Climate*, 32(15), 4783-4803.
- Perlin, N., Skillingstad, E. D., Samelson, R. M., & Barbour, P. L. (2007). Numerical simulation of air–sea coupling during coastal upwelling. *Journal of Physical Oceanography*, 37(8), 2081-2093.
- Pohl, B., Rouault, M., & Roy, S. S. (Accepted/In press). Simulation of the annual and diurnal cycles of rainfall over South Africa by a regional climate model. *Climate Dynamics*, 1-20. <https://doi.org/10.1007/s00382-013-2046-8><https://protect-za.mimecast.com/s/Zw4YC2Rq5WiO2OYJsn2hOC>
- Pohl, B., Fauchereau, N., Richard, Y., Rouault, M., & Reason, C.J.C. (2009). Interactions between synoptic, intraseasonal and interannual convective activity over Southern Africa. *Climate Dynamics*, 33, 1033-1050.

838 Ratna, S. B., J. V. Ratnam, S. K. Behera, C. J. de W. Rautenbach, T. Ndarana, K. Takahashi, and
839 T. Yamagata, 2014: Performance assessment of three convective parameterization
840 schemes in WRF for downscaling summer rainfall over South Africa. *Climate Dyn.*, 42,
841 2931–2953, doi:<https://doi.org/10.1007/s00382-013-1918-2><[https://protect-](https://protect-za.mimecast.com/s/iNwJC3lr5wi0g0kJSq_pPY)
842 [za.mimecast.com/s/iNwJC3lr5wi0g0kJSq_pPY](https://protect-za.mimecast.com/s/iNwJC3lr5wi0g0kJSq_pPY)>
843

844 Ratnam, J. V., Y. Morioka, S. K. Behera, and T. Yamagata, 2015: A model study of regional air–
845 sea interaction in the austral summer precipitation over southern Africa. *J. Geophys.*
846 *Res. Atmos.*, 120, 2342–2357,
847 doi:<https://doi.org/10.1002/2014JD022154><[https://protect-za.mimecast.com/s/](https://protect-za.mimecast.com/s/YsmPC48v7LU323VQIB5omy)
848 [YsmPC48v7LU323VQIB5omy](https://protect-za.mimecast.com/s/YsmPC48v7LU323VQIB5omy)>
849

850 Reason, C. J. C., & Jury, M. R. (1990). On the generation and propagation of the southern
851 African coastal low. *Quarterly Journal of the Royal Meteorological Society*, 116(495),
852 1133–1151.
853

854 Reason, C. J. C. (1998). Warm and cold events in the southeast Atlantic/southwest Indian
855 Ocean region and potential impacts on circulation and rainfall over southern Africa.
856 *Meteorology and Atmospheric Physics*, 69(1-2), 49–65.
857

858 Reason, C. J. C., & Mulenga, H. (1999). Relationships between South African rainfall and SST
859 anomalies in the southwest Indian Ocean. *International Journal of Climatology: A*
860 *Journal of the Royal Meteorological Society*, 19(15), 1651–1673.
861

862 Reason, C. J. C., Allan, R. J., Lindesay, J. A., & Ansell, T. J. (2000). ENSO and climatic signals
863 across the Indian Ocean basin in the global context: Part I, Interannual composite
864 patterns. *International Journal of Climatology*, 20(11), 1285–1327.
865

866 Reason, C. J. C. (2001). Subtropical Indian Ocean SST dipole events and southern African
867 rainfall. *Geophysical Research Letters*, 28(11), 2225–2227.
868

869 Reason, C. J. C., Hachigonta, S., & Phaladi, R. F. (2005). Interannual variability in rainy season
870 characteristics over the Limpopo region of southern Africa. *International Journal of*
871 *Climatology*, 25(14), 1835–1853.
872

873 Reason, C. J. C., & Jagadheesha, D. (2005). A model investigation of recent ENSO impacts
874 over southern Africa. *Meteorology and Atmospheric Physics*, 89(1-4), 181–205.
875

876 Reason, C. J. C., Landman, W., & Tennant, W. (2006). Seasonal to decadal prediction of
877 southern African climate and its links with variability of the Atlantic Ocean. *Bulletin of*
878 *the American Meteorological Society*, 87(7), 941–955.
879

880 Renault, L., Molemaker, M. J., McWilliams, J. C., Shchepetkin, A. F., Lemarié, F., Chelton, D., ...
881 & Hall, A. (2016). Modulation of wind work by oceanic current interaction with the at-
882 mosphere. *J. Phys. Oc.*, 46(6), 1685–1704.
883

- Renault, L., McWilliams, J. C., & Penven, P. (2017). Modulation of the agulhas current retroflection and leakage by oceanic current interaction with the atmosphere in coupled simulations. *Journal of Physical Oceanography*, 47(8), 2077-2100.
- Rouault, M., White, S. A., Reason, C. J. C., Lutjeharms, J. R. E., & Jobard, I. (2002). Ocean-atmosphere interaction in the Agulhas Current region and a South African extreme weather event. *Weather and Forecasting*, 17(4), 655-669.
- Rouault, M., Florenchie, P., Fauchereau, N., & Reason, C. J. (2003). South East tropical Atlantic warm events and southern African rainfall. *Geophysical Research Letters*, 30(5).
- Sardeshmukh, P. D., & Hoskins, B. I. (1984). Spatial smoothing on the sphere. *Monthly weather review*, 112(12), 2524-2529.
- Singleton, A. T., & Reason, C. J. C. (2007). Variability in the characteristics of cut-off low pressure systems over subtropical southern Africa. *International Journal of Climatology: A Journal of the Royal Meteorological Society*, 27(3), 295-310.
- Skamarock, W. C., Klemp, J. B., Dudhia, J., Gill, D. O., Barker, D. M., Wang, W., & Powers, J. G. (2005). *A description of the advanced research WRF version 2* (No. NCAR/TN-468+ STR). National Center For Atmospheric Research, Boulder Colorado, Mesoscale and Microscale Meteorology Div.
- Shannon, L. V., Boyd, A. J., Brundrit, G. B., & Taunton-Clark, J. (1986). On the existence of an El Niño-type phenomenon in the Benguela system. *Journal of Marine Research*, 44(3), 495-520.
- Stark, J. D., Donlon, C. J., Martin, M. J., & McCulloch, M. E. (2007, June). OSTIA: An operational, high resolution, real time, global sea surface temperature analysis system. In *Oceans 2007-Europe* (pp. 1-4). IEEE.
- Todd, M., & Washington, R. (1999). Circulation anomalies associated with tropical-temperate troughs in southern Africa and the south west Indian Ocean. *Climate Dynamics*, 15(12), 937-951.
- Tyson, P. D., & Preston-Whyte, R. A. (2000). *Weather and climate of southern Africa*. Oxford University Press.
- Usman, M. T., & Reason, C. J. C. (2004). Dry spell frequencies and their variability over southern Africa. *Climate research*, 26(3), 199-211.
- Veitch, J. A., Florenchie, P., & Shillington, F. A. (2006). Seasonal and interannual fluctuations of the Angola-Benguela Frontal Zone (ABFZ) using 4.5 km resolution satellite imagery from 1982 to 1999. *International Journal of Remote Sensing*, 27(05), 987-998.
- Walker, N. D., & Mey, R. D. (1988). Ocean/atmosphere heat fluxes within the Agulhas Retroflection region. *Journal of Geophysical Research: Oceans*, 93(C12), 15473-15483.

- 932 Walker, N. D. (1990). Links between South African summer rainfall and temperature variabil-
933 ity of the Agulhas and Benguela Current systems. *Journal of Geophysical Research:*
934 *Oceans*, 95(C3), 3297-3319.
935
- 936 Weldon, D., & Reason, C. J. C. (2014). Variability of rainfall characteristics over the South
937 Coast region of South Africa. *Theoretical and applied climatology*, 115(1-2), 177-185.
938
- 939 Wilcoxon, F. (1945) Individual Comparisons by Ranking Methods. *Biometrics Bulletin*, 1, 80-
940 83. <http://dx.doi.org/10.2307/3001968>
941
- 942 Woollings, T., Hoskins, B., Blackburn, M., Hassell, D., & Hodges, K. (2010). Storm track sensi-
943 tivity to sea surface temperature resolution in a regional atmosphere model. *Climate*
944 *dynamics*, 35(2-3), 341-353.
945

946

948 **Table I:** Details of all simulations

949

Simulations	<i>CTRL</i>	<i>SMTH</i>	<i>HR-ABFZ</i>	<i>SMTH-ABFZ</i>
Period	1 Sept 2008- 1 May 2009	1 Oct 2008- 1 May 2009	1 Oct 2008- 1 May 2009	1 Oct 2008- 1 May 2009
Ensemble-member	5	5	5	5
Restart set on the 1 st Sept. 2008	29 and 30 Sept. 2008 1 st ,2nd and 3th Sept. 2008	From CTRL: 29 and 30 Sept. 2008 1 st ,2nd and 3th Sept. 2008	From CTRL: 29 and 30 Sept. 2008 1 st ,2nd and 3th Sept. 2008	From CTRL: 29 and 30 Sept. 2008 1 st ,2nd and 3th Sept. 2008
SST fronts	Sharp	Smoothed	Sharp in the ABFZ box and smoothed outside	Smoothed in the ABFZ box and sharp outside

950

Figures and Tables

Figure 1: ERA-Interim based schematic showing the important low-level atmospheric and oceanic features of southern Africa during austral summer (*DJF*). The mean vertically-integrated moisture flux (surface to 850hPa) is represented by grey arrows, while the green arrows summarize the important directions of the key low-level moisture fluxes. The mean position of *ITCZ* is represented by the thick dotted purple line. The Angola Low is denoted by the letter L, which is shown through the geopotential height at 850 hPa that is higher than 1490m being marked with blue dots. The orange contours represent the subtropical highs over the Atlantic and Indian Oceans. Cool and warm ocean areas are shown through the 18°, 20°, 22° and 24°C contours of *SST* (shaded blue) and the black contours its standard deviation. Also illustrated is the location of the influential Agulhas Current and its retroflection (red line), and the *ABFZ* (represented by a blue-red line) separating the so-called warm and cool oceans in the southeast Atlantic (the delimitation follows here the 22°C SST contour at about 16°S). Locations of considerable topography are contoured in brown. The cloud symbols refer to the tropical-extratropical cloud bands that typically extend from the *AL* over subtropical southern Africa. The black frame represents the domain of all WRF simulations. The *ABFZ* box (highlighted in blue) is where the forcing *SST* has been replaced in the *HR-ABFZ* and *LR-HBFZ* experiments (see *Section 3* for details).

Figure 2: Snapshot of *SST* (°C) on 12 January 2009 at 12h00 UCT for (a) the *CRTL*, (b) *SMTH*, (c) *HR-ABFZ* and (d) *SMTH-ABFZ* forcing fields. The *ABFZ* domain where the *SST* is modified is represented by the white box.

Figure 3: (a) The *DJF CTRL* ensemble-mean of 800 hPa geopotential height [shaded; in meters] and associated moisture fluxes (arrows). (b) *DJF* ensemble-mean of 800 hPa geopotential height [contours, in meters]. For clarity, note that the 800 hPa contours outside of the mean location of the *AL* have been masked. The dark blue dotted areas correspond to locations where grid points are flagged as having rainfall for more than 10% of the full simulation period (see text for details). The standard deviation of the *SST* forcing are contoured from 1.6° to 3°C every 0.2°C. The arrows correspond to the *DJF* ensemble-mean of the vertically-integrated moisture flux from the surface to 800 hPa. Note that only

983 the main regions of incoming fluxes from the oceans are plotted (i.e., tropical Atlantic and
984 Indian Oceans, and over the Mozambique Channel).

985

986 **Figure 4:** (a) 30-day window running-mean of the minimum of the geopotential height
987 at 800 hPa in the *CTRL* (black line) over the AL domain. (b) Phase of low with the 30-day
988 window running mean of the number of Tropical lows (blue shade) and Heat lows (red
989 shade) for *CTRL*. (c) Ratio between the numbers of Tropical Lows detected over the total
990 number of AL events (see text for details) in black. The shaded areas on the three panels
991 correspond to +/- 1 std. dev. of the ensemble-mean of the *CTRL* simulations.

992

993 **Figure 5:** (a) DJF ensemble-mean 800hPa geopotential height for the *CTRL* (contour in
994 black), (b) *SMTH* (contour in red), (c) *SMTH-ABFZ* (contour in blue) and (d) *HR-ABFZ* (contour
995 in green). Note that for comparison purposes, the contour lines of the *CTRL* have also been
996 drawn on the panels (b) and (c), while the contour lines of the *SMTH* are also shown on
997 panel (d). The black dots denote non-significant difference the two geopotential times
998 series (i.e., the sensitivity and its relative reference) performed by a student test at 90% of
999 confidence level.

1000

1001 **Figure 6:** 30-day window running mean (line) and the corresponding standard
1002 deviation (shaded) of the minimum of 800hPa geopotential height in the AL region of (a)
1003 *CTRL* and *SMTH* (black and red lines, respectively), (b) *CTRL* and *SMTH-ABFZ* (black and blue
1004 lines, respectively) and (c) *SMTH* and *HR-ABFZ* (red and green lines, respectively),
1005 respectively.

1006

1007 **Figure 7:** Snapshot of the SST gradient corresponding to the (a) *CTRL* and the (b)
1008 *SMTH* SST forcing around the ABFZ box, respectively. (c) The spatial power spectra
1009 [arbitrary units] of the *CTRL* (black) and *SMTH* (red) SST gradient in the ABFZ box during the
1010 entire simulation. The thick line corresponds to an average of each time step spectra while
1011 the thin one correspond to the one exhibit on panels (a) and (b).

1012

1013 **Figure 8:** Boxplot of the maximum of the filtered vorticity during each events of

1014 all ensemble-members. Statistical results are significant at 90% of confidence level. Please,
1015 refer to the text for more details.

1016

1017 **Figure 9:** Composite of the moisture flux (arrows, g/kg m/s), daily rainfall (shaded) and
1018 OLR values (black dots where OLR mean value is below 250 W/m^2) the following time step
1019 of each TL genesis for the $CTRL$ ensemble-mean simulations.

1020

1021 **Figure 10:** Anomalies of the composite of daily rainfall associated with TL events
1022 between $CTRL$ and $SMTH$ (a), $CTRL$ and $SMTH-ABFZ$ (b) and $SMTH$ and $HR-ABFZ$ (c),
1023 respectively. Anomalies for which the Wilcoxon signed rank test p-value [Wilcoxon, 1945]
1024 are larger than 0.05 are displayed, the remaining areas are shown in hatching.

1025

1026 **Figure 11:** Ensemble-mean of wet $spell$ events in the $CTRL$

1027

1028 **Figure 12:** The difference in the DJF wet $spell$ events between (a) $CTRL$ and $SMTH$, (b)
1029 $CTRL$ and $SMTH-ABFZ$ and (c) $SMTH$ and $HR-ABFZ$, respectively.

1030

1031

- 1032 **Acronym list:**
- 1033 **ABFZ:** Angola-Benguela Frontal Zone
- 1034 **AL:** Angola-Low
- 1035 **BUS:** Benguela Upwelling System
- 1036 **DJF:** Austral summer months: December-January-February.
- 1037 **ERA-Interim:** European Reanalysis developed at ECMWF
- 1038 **ECMWF:** European Centre for Medium-Range Weather Forecasts
- 1039 **ENSO:** El-Nino Southern Oscillation
- 1040 **HL:** Heat Low
- 1041 **ITCZ:** Inter-Tropical Convergence Zone
- 1042 **MABL:** Marine Atmospheric Boundary Layer
- 1043 **NCEP:** National Centers for Environmental Prediction
- 1044 **NCEP-FNL:** NCEP Final Reanalysis
- 1045 **OLR:** Ongoing Longwave Radiation
- 1046 **OSTIA:** Operational Sea Surface Temperature and Sea Ice Analysis
- 1047 **PBL:** Planetary Boundary Layer
- 1048 **SST:** Sea Surface Temperature
- 1049 **TL:** Tropical Low
- 1050 **WRF:** Weather Research and Forecasting model

Figure 1

ERA-I based schematic of low-level atmosphere and ocean surface layer dynamics
Southern Africa austral summer

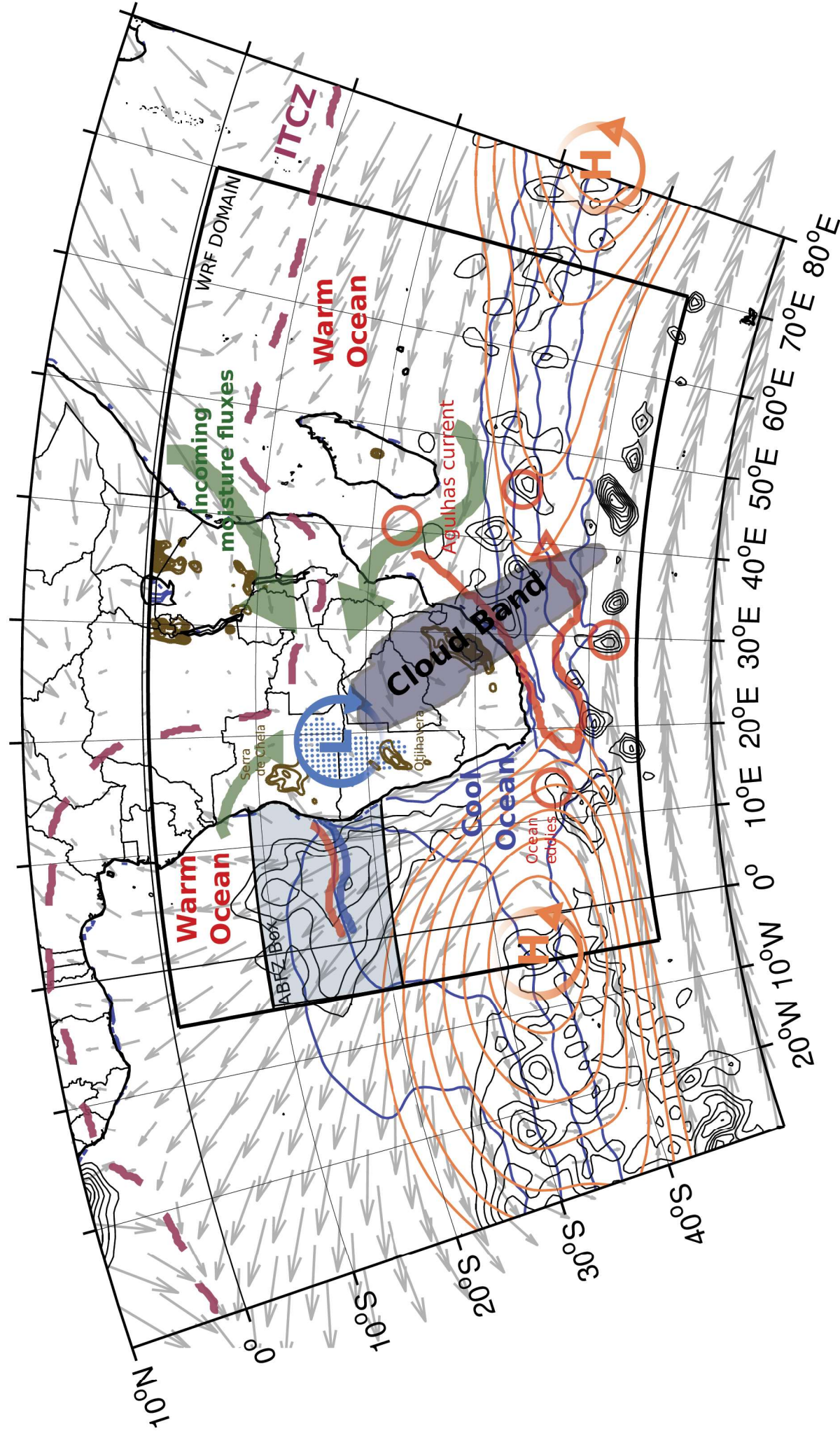


Figure 2

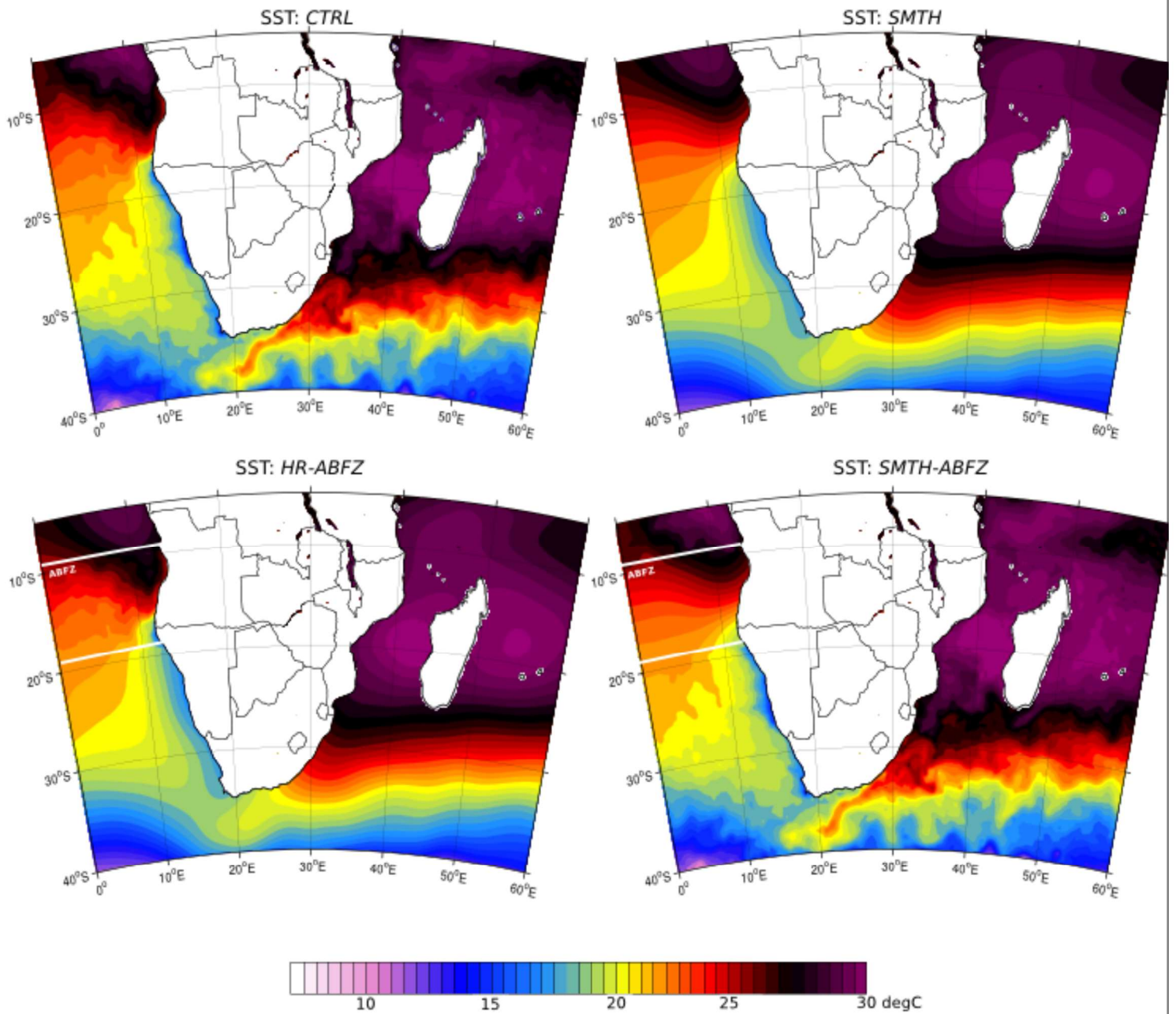


Figure 2: Snapshot of SST ($^{\circ}\text{C}$) on 12 January 2009 at 12h00 UCT for (a) the CTRL, (b) SMTH, (c) HR-ABFZ and (d) SMTH-ABFZ forcing fields. The ABFZ domain where SSTs are modified are represented by the white box.

Figure 3a
Figure 3a

CTRL DJF Ensemble-mean
800 hPa geopotential height and moisture fluxes

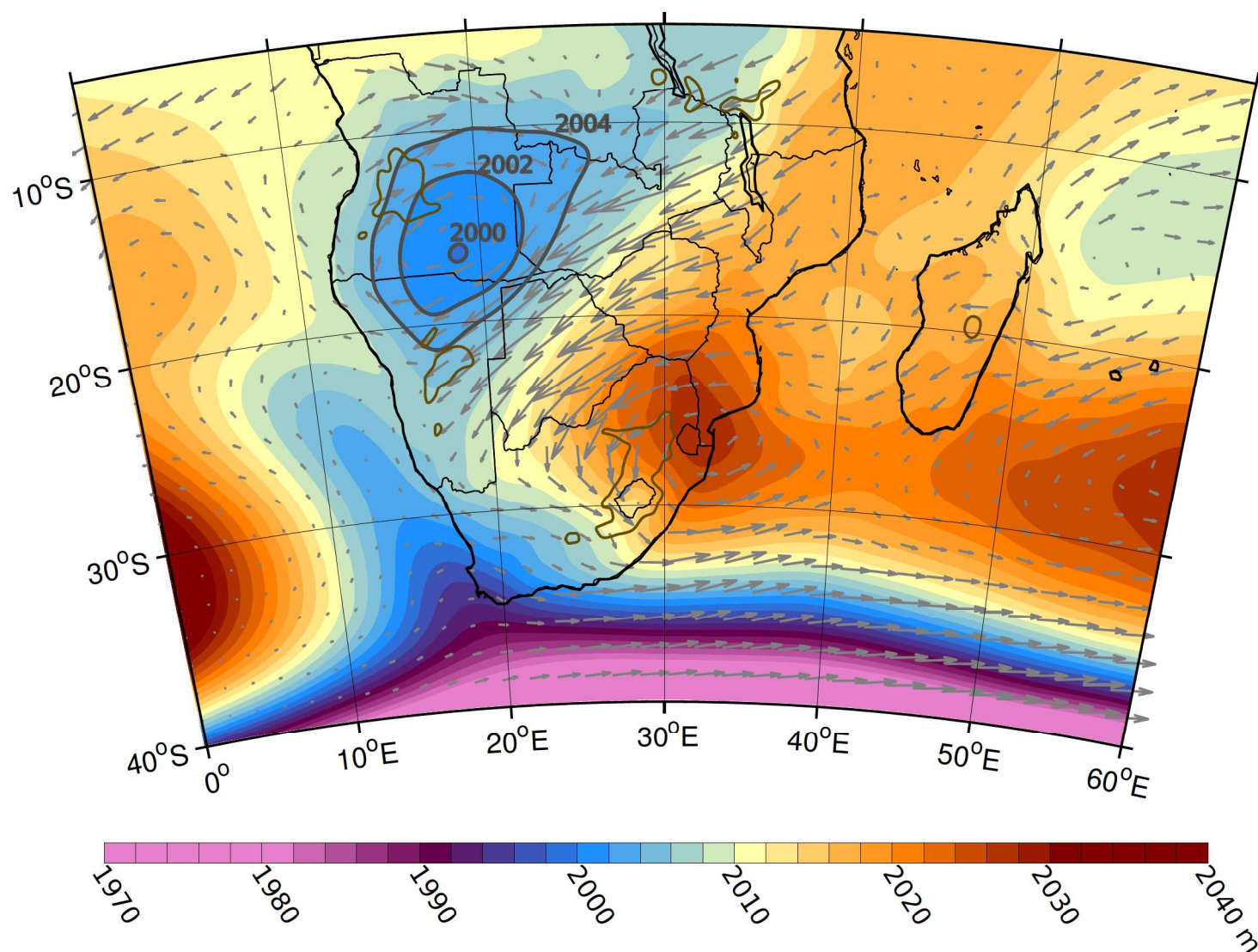


Figure 3: (a) The DJF CTRL ensemble-mean of 800 hPa geopotential height [shaded; in meters] and associated moisture fluxes (arrows). (b) DJF ensemble-mean of 800 hPa geopotential height [contours, in meters]. For clarity, note that the 800 hPa contours have outside of the mean location of the AL have been masked. The dark blue dotted areas correspond to locations where grid points are flagged as having rainfall for more than 10% of the full simulation period (see text for details). The standard deviation of the SST forcing are contoured from 1.6° to 3°C every 0.2°C. The arrows correspond to the DJF ensemble-mean of the vertically-integrated moisture flux from the surface to 800 hPa. Note that only the main regions of incoming fluxes from the oceans are plotted (i.e., tropical Atlantic and Indian Oceans, and over the Mozambique Channel).

Figure 3b

Figure 3b

Ensemble-mean *CTRL*

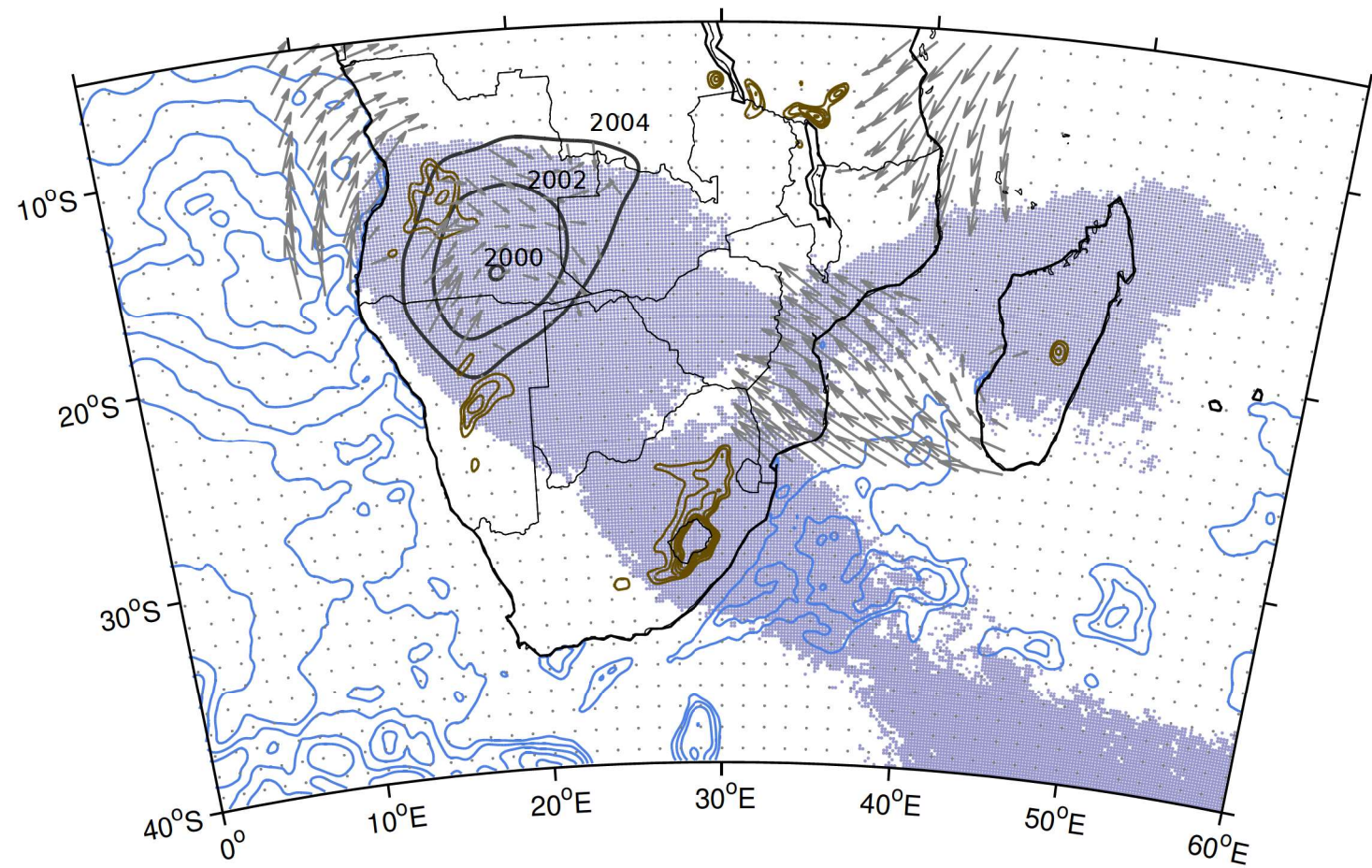


Figure 4

Figure 4

Figure 4: (a) 30-day window running-mean of the minimum of the geopotential height at 800 hPa in the CTRL (black line) over the AL domain. (b) Phase of low with the 30-day window running mean of the number of Tropical lows (blue shade) and Heat lows (red shade) for CTRL. (c) Ratio between the numbers of Tropical Lows detected over the total number of AL events (see text for details) in black. The shaded areas on the three panels correspond to ± 1 std. dev. of the ensemble-mean of the CTRL simulations.

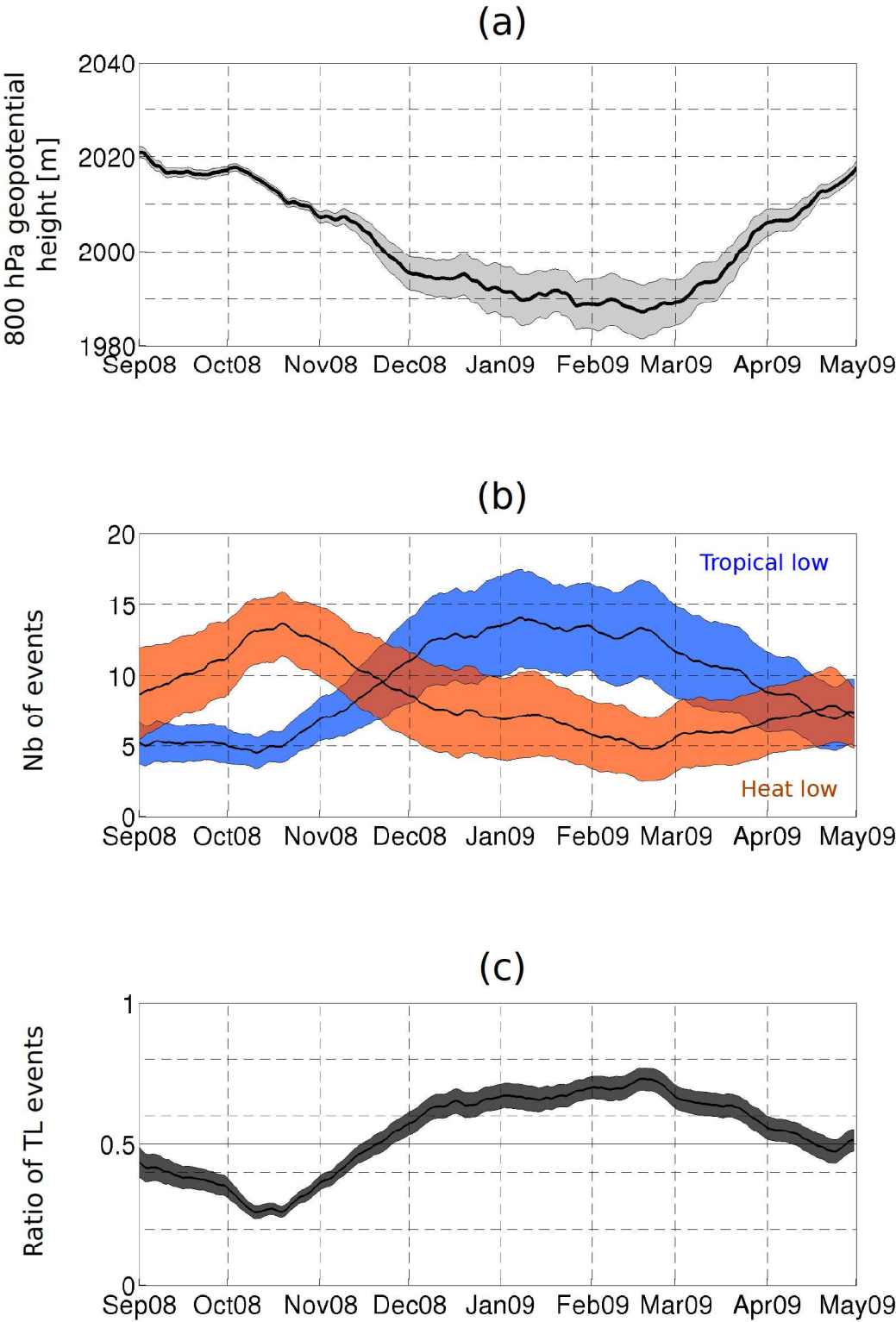
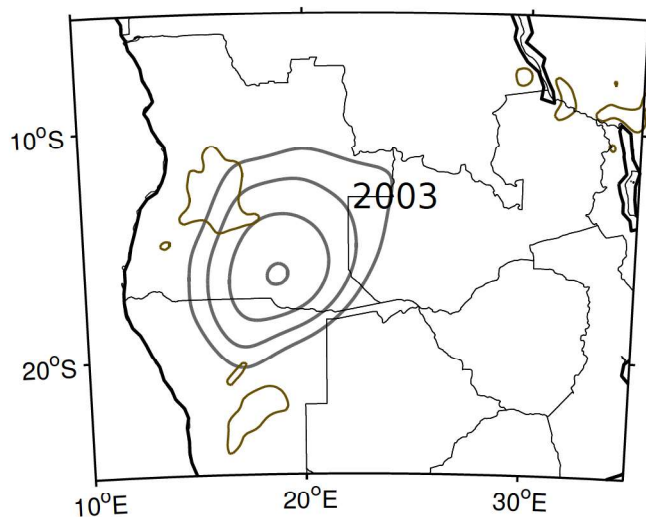


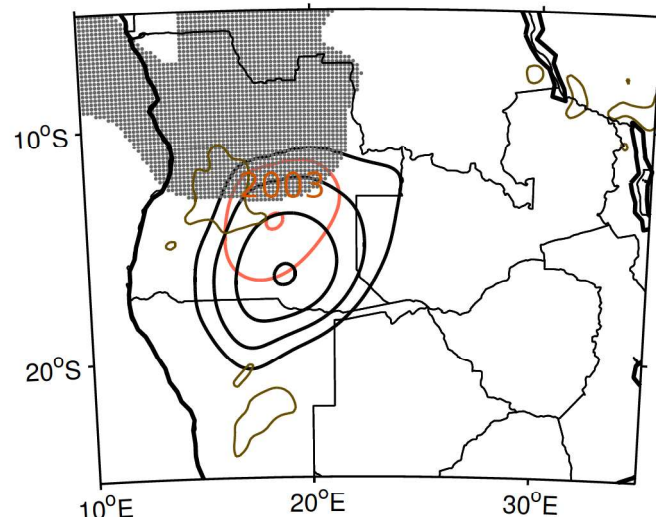
Figure 5

Figure 5

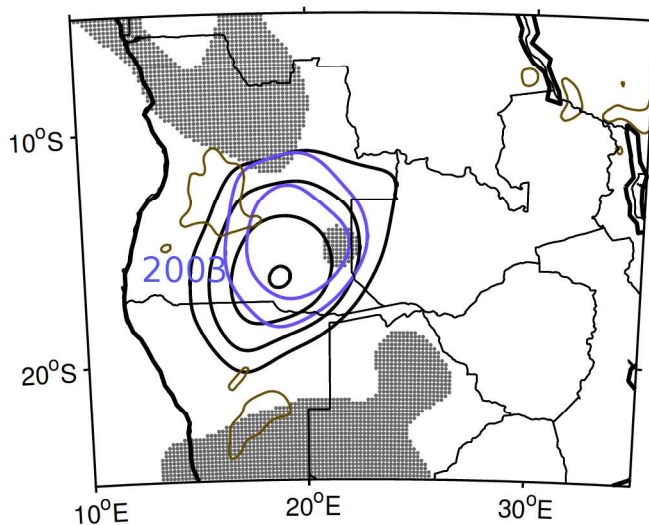
(a) *CTRL*
DJF Ensemble-mean



(b) *SMTH*
DJF Ensemble-mean



(c) *SMTH-ABFZ*
DJF Ensemble-mean



(d) *HR-ABFZ*
DJF Ensemble-mean

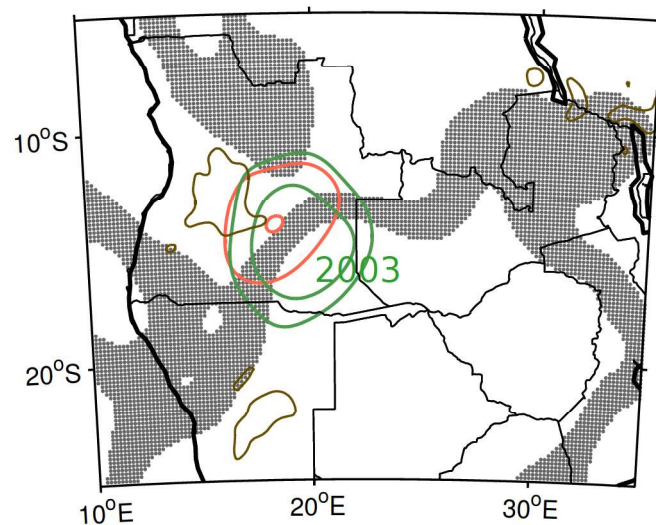
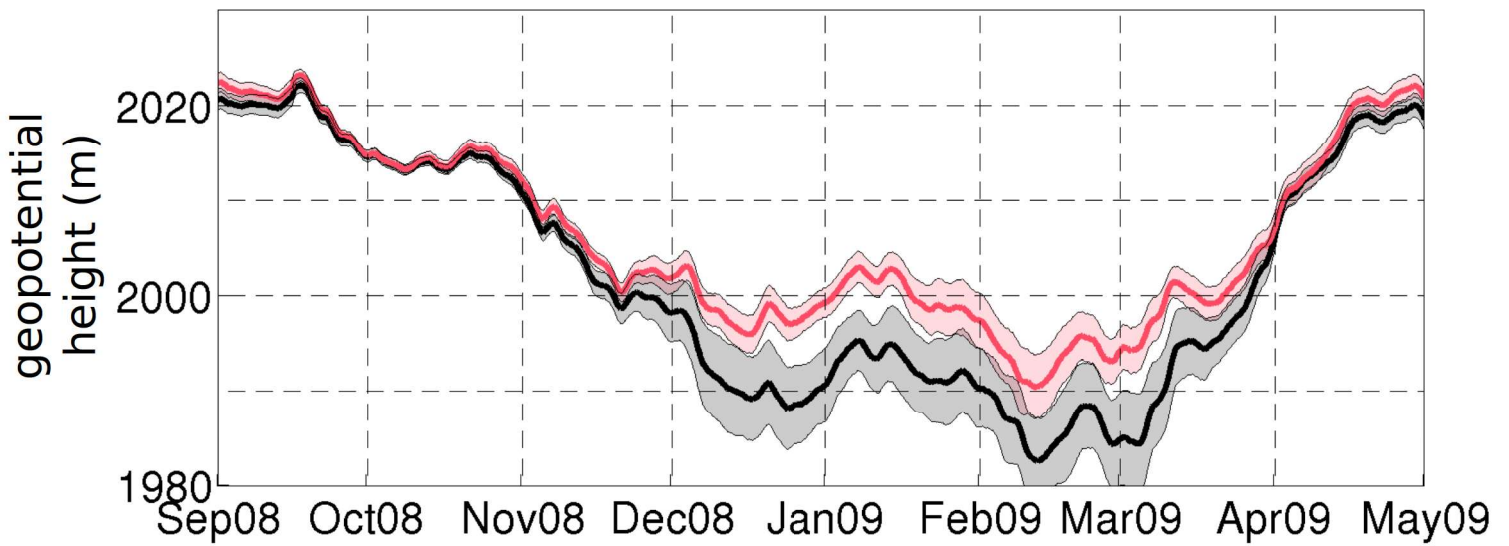


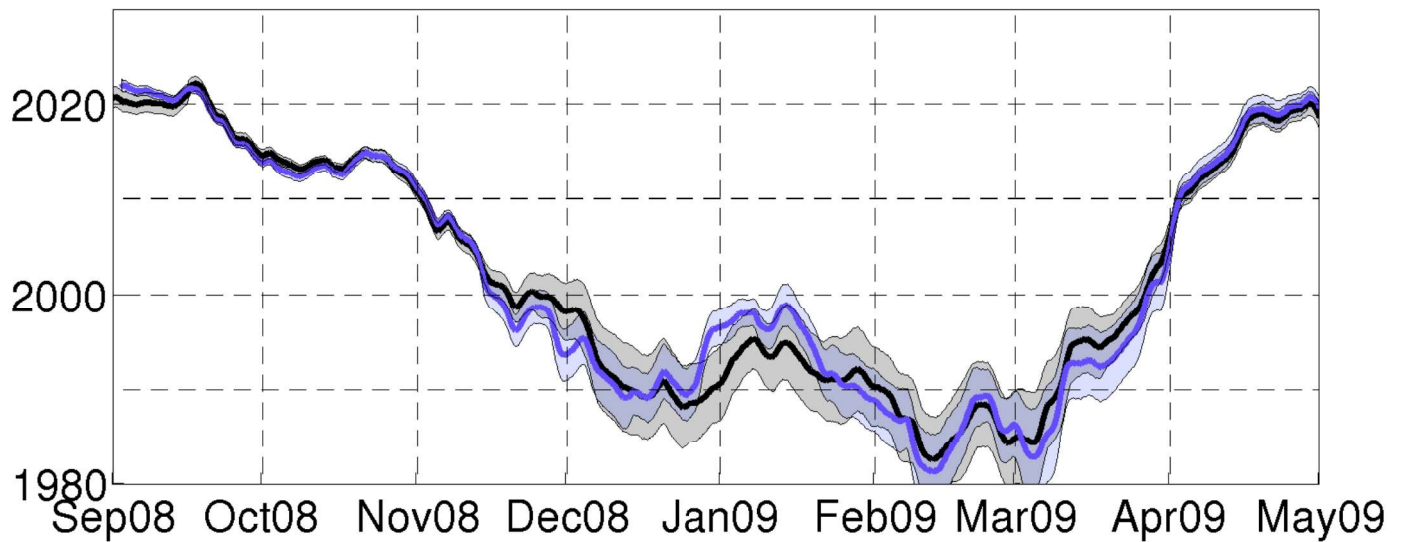
Figure 5: (a) DJF ensemble-mean 800hPa geopotential height for the CTRL (contour in black), (b) SMTH (contour in red), (c) SMTH-ABFZ (contour in blue) and (d) HR-ABFZ (contour in green). Note that for comparison purposes, the contour lines of the CTRL have also been drawn on the panels (b) and (c), while the contour lines of the SMTH are also shown on panel (d). The black dots denote non-significant difference the two geopotential times series (i.e., the sensitivity and its relative reference) performed by a student test at 90% of confidence level.

Figure 6

(a) Minimum of 800 hPa gph
CTRL vs *SMTH*



(b) Minimum of 800 hPa gph
CTRL vs *SMTH-ABFZ*



(c) Minimum of 800 hPa gph
SMTH vs *HR-ABFZ*

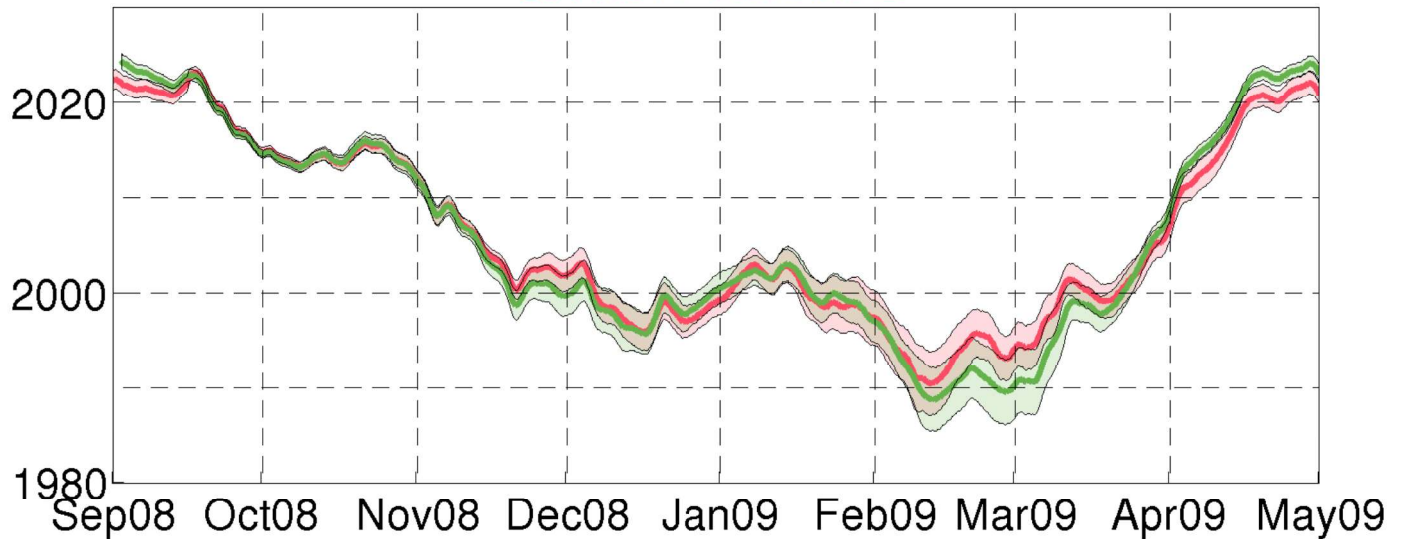
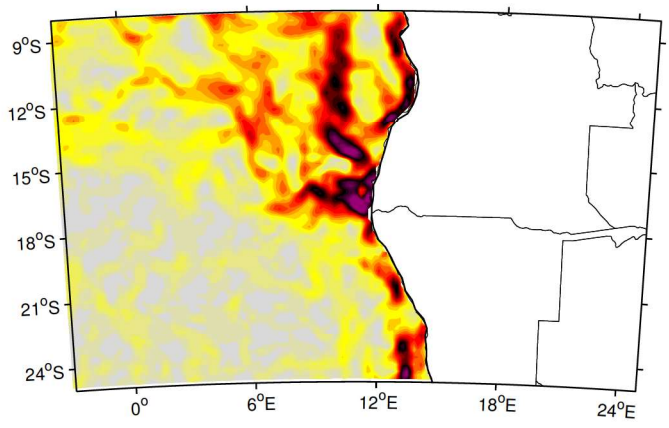


Figure 6: 30-day window running mean (line) and the corresponding standard deviation (shaded) of the minimum of 800hPa geopotential height in the AL region of (a) CTRL and SMTH (black and red lines, respectively), (b) CTRL and SMTH-ABFZ (black and blue lines, respectively) and (c) SMTH and HR-ABFZ (red and green lines, respectively), respectively.

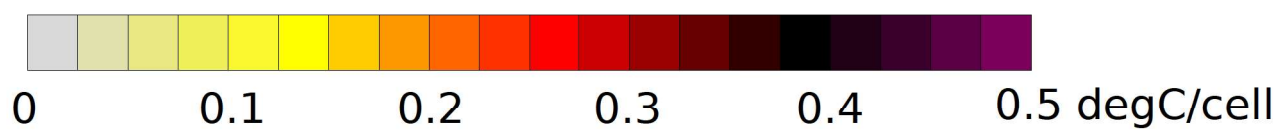
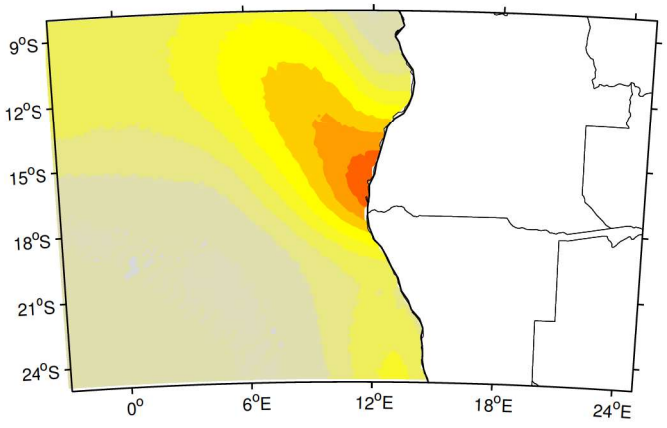
Figure 7

Figure 7 Figure 7: Snapshot of the SST gradient corresponding to the (a) CTRL and the (b) SMTH SST forcing around the ABFZ box, respectively. (c) The spatial power spectra of the CTRL (black) and SMTH (red) SST gradient in the ABFZ box during the entire simulation. The thick line correspond to an average of each time step spectra while the thin one correspond to the one exhibit on panels (a) and (b).

(a) CTRL SST gradient



(b) SMTH SST gradient



(c) Power spetrum SST gradient

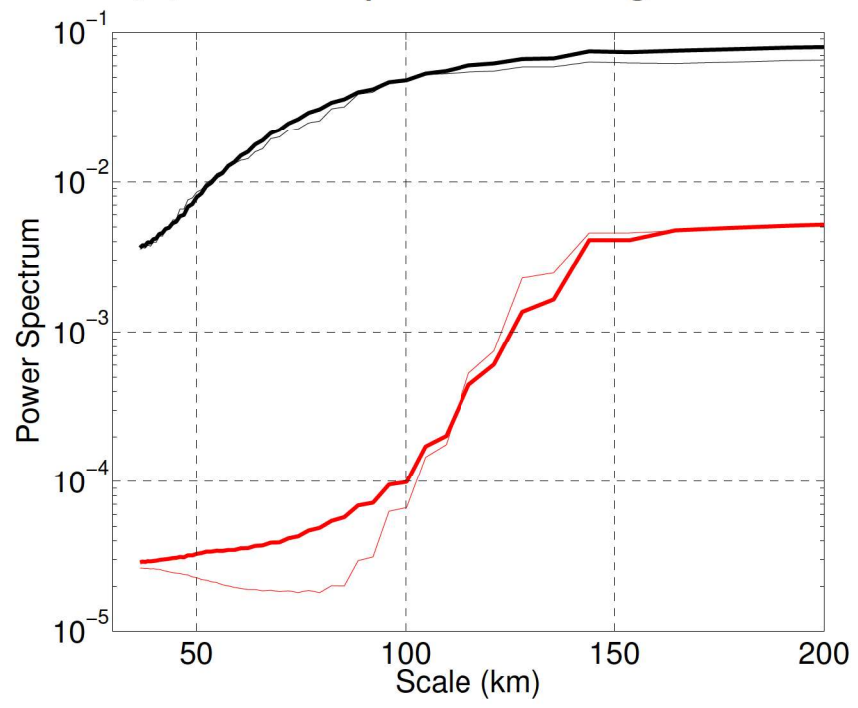


Figure 8

Figure 8: Boxplot of the maximum of the filtered vorticity during each events of all ensemble-members. Statistical results are significant at 90% of confidence level. Please, refer to the text for more details.

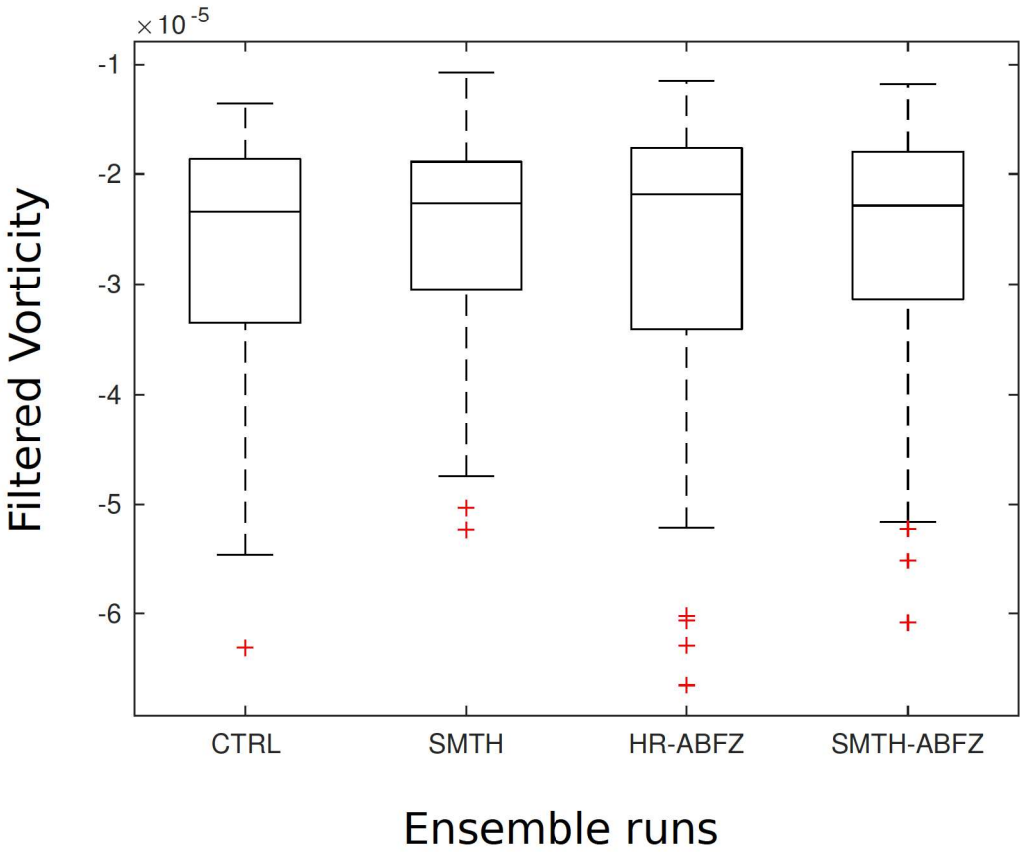


Figure 9
Figure 9

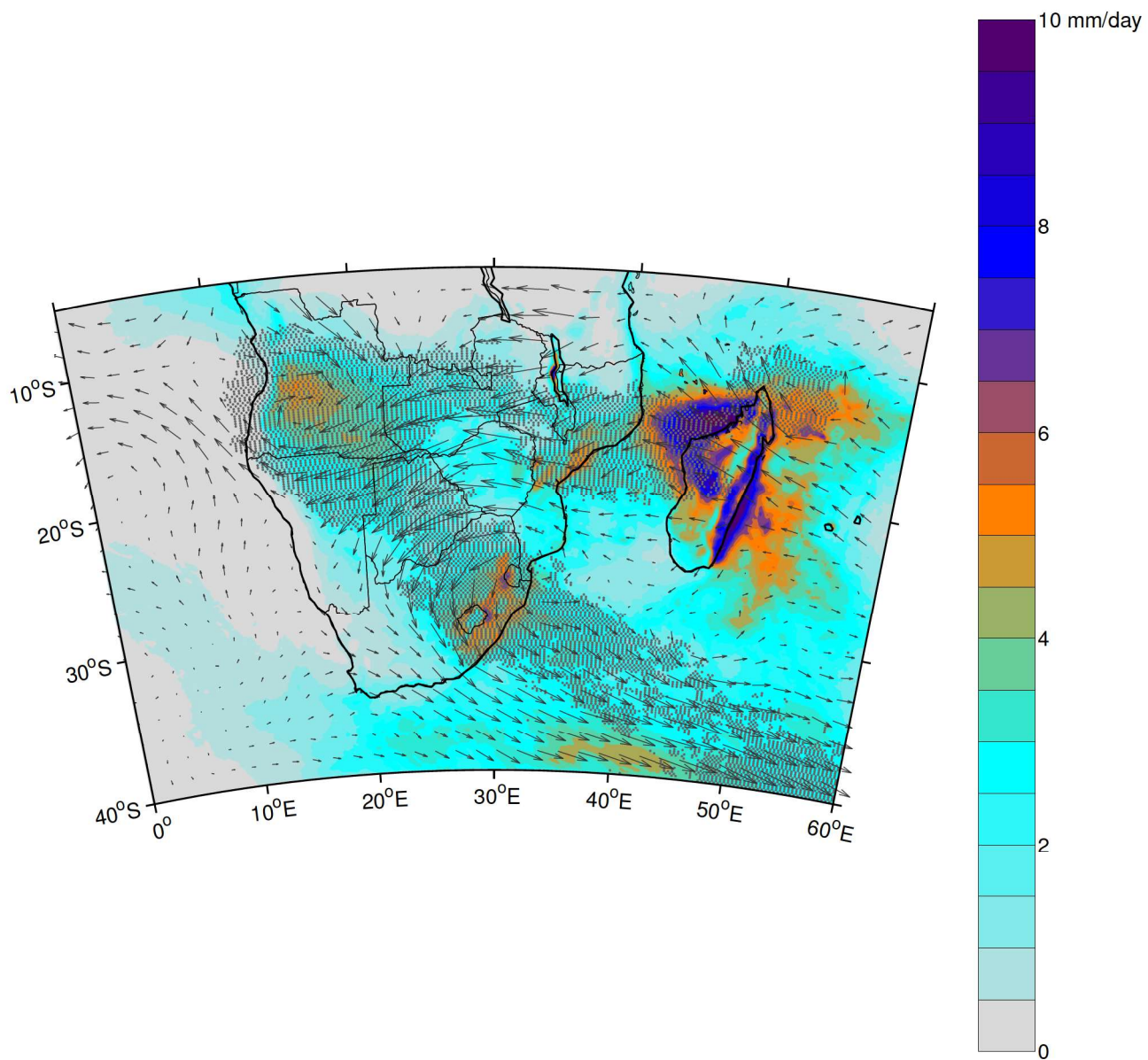


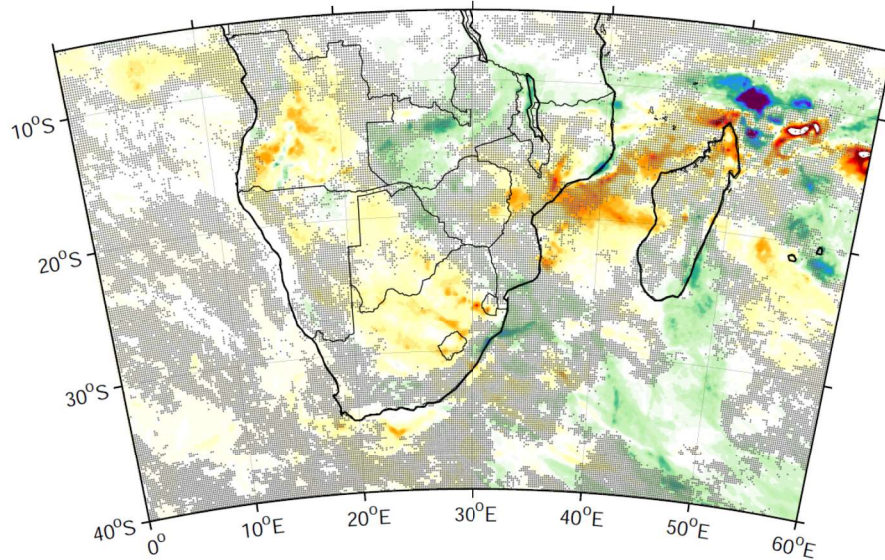
Figure 9: Composite of the moisture flux (arrows), daily rainfall (shaded) and OLR values (black dots where OLR mean value is below 250 W/m²) the following time step of each TL genesis for the CTRL ensemble-mean simulations.

Figure 10

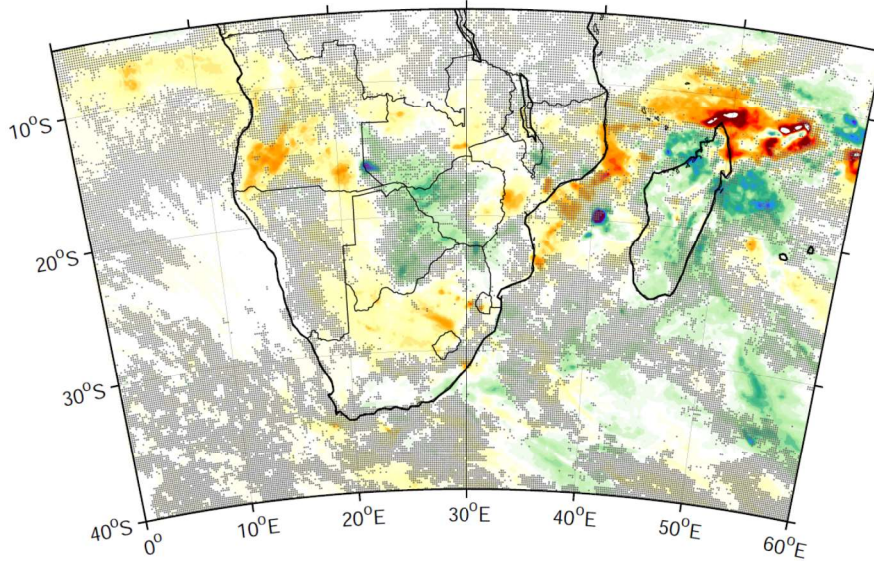
Figure 10

Figure 10: Anomalies of the composite of daily rainfall associated with TL events between CTRL and SMTH (a), CTRL and SMTH-ABFZ (b) and SMTH and HR-ABFZ (c), respectively. Anomalies for which the Wilcoxon signed rank test p-value [Wilcoxon, 1945] are larger than 0.05 are displayed, the remaining areas are shown in hatching.

(a) Composite *SMTH - CTRL*



(b) Composite *SMTH-ABFZ - CTRL*



(c) Composite *HR-ABFZ - SMTH*

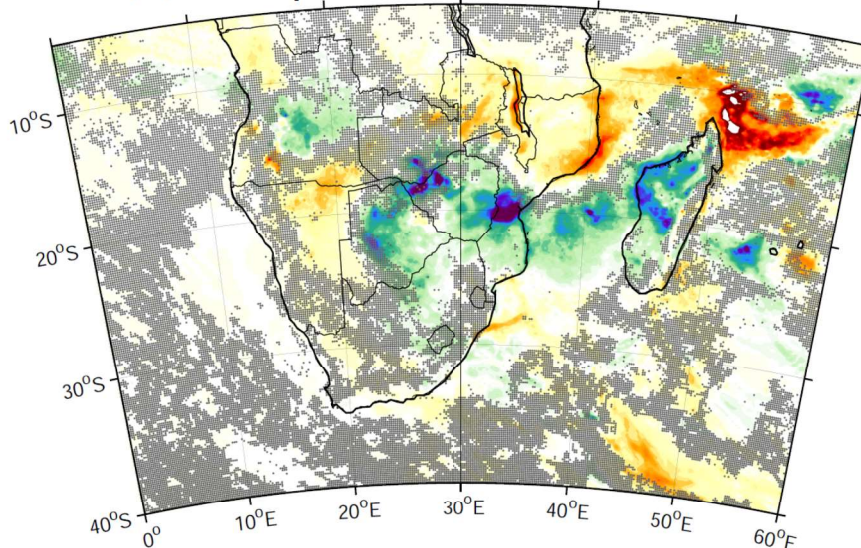


Figure 11
Figure 11

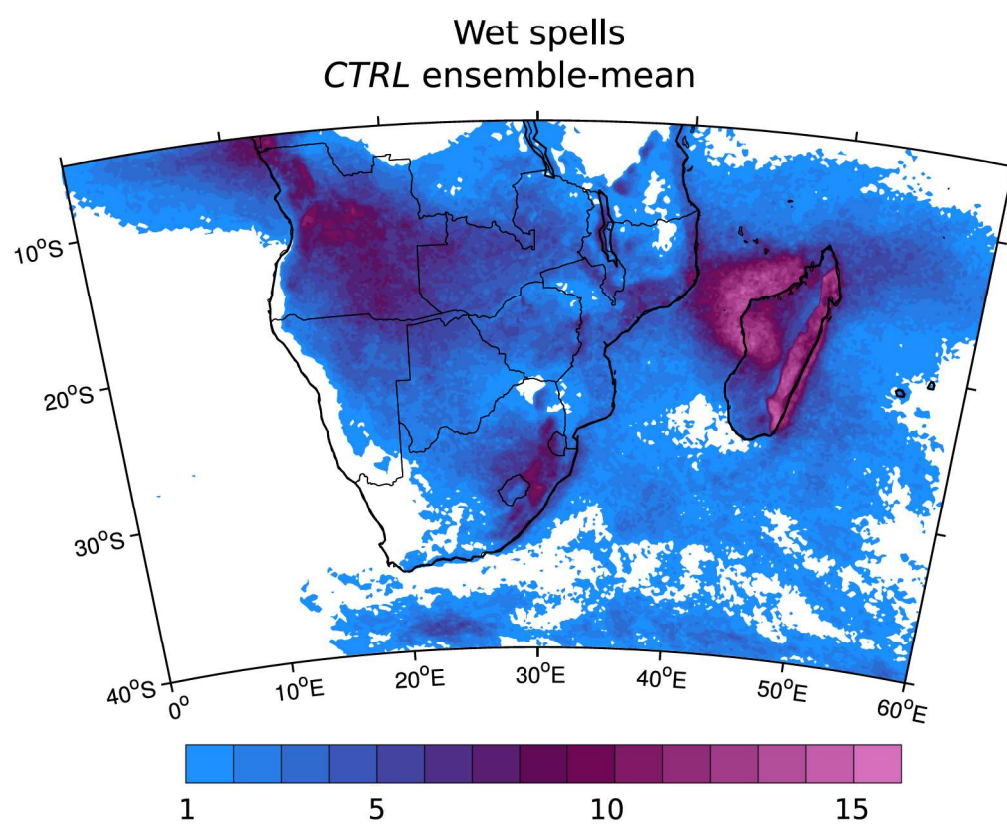
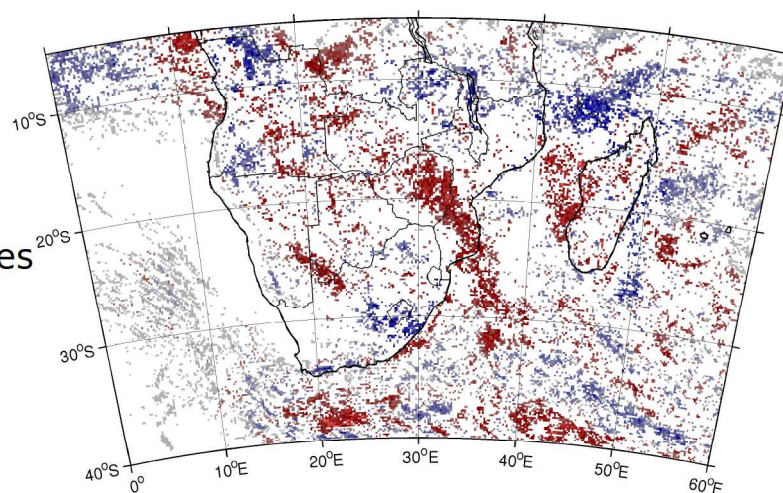


Figure 11: Ensemble-mean of wet and events in the CTRL

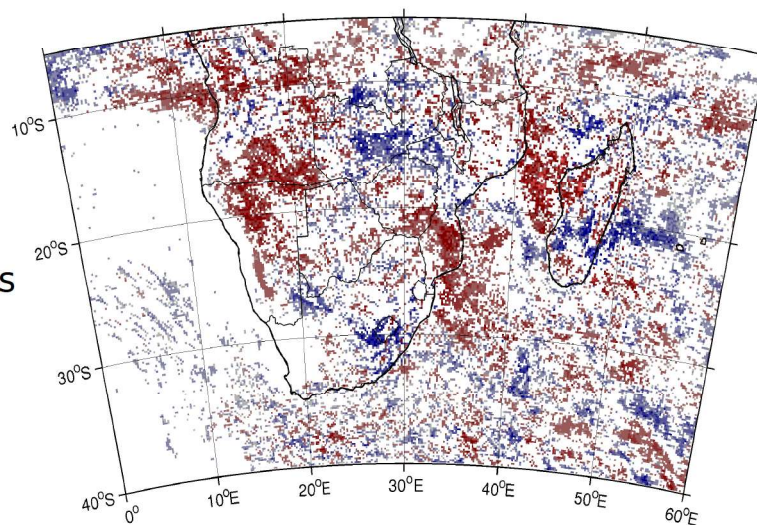
Figure 12

Figure 12 : The difference in the DJF wet spell anomalies between (a) CTRL and SMTH, (b) CTRL and SMTH-ABFZ and (c) SMTH and HR-ABFZ , respectively.

(a) wet spell anomalies
SMTH - CTRL



(b) wet spell anomalies
SMTH-ABFZ - CTRL



(c) wet spell anomalies
HR-ABFZ - SMTH

